

TRISO particle fuel performance and failure analysis with BISON

Wen Jiang^{a,*}, Jason D. Hales^a, Benjamin W. Spencer^a, Blaise P. Collin^c,
Andrew E. Slaughter^b, Stephen R. Novascone^a, Aysenur Toptan^a, Kyle A. Gamble^a,
Russell Gardner^c

^a Idaho National Laboratory, Computational Mechanics & Materials Department, P.O. Box 1625, Idaho Falls, ID 83415, United States

^b Idaho National Laboratory, Computational Frameworks, P.O. Box 1625, Idaho Falls, ID 83415, United States

^c Kairos Power LLC, 707 W. Tower Avenue, Alameda, CA 94501, United States

ARTICLE INFO

Article history:

Received 22 October 2020

Revised 11 December 2020

Accepted 5 January 2021

Available online 26 January 2021

Keywords:

BISON

TRISO

UCO

Failure analysis

Fission product release

ABSTRACT

Because of its widespread use in multiple advanced reactor concepts, the ability to accurately simulate tri-structural isotropic (TRISO) fuel performance is essential for ensuring the safe operation of these reactors. To that end, the BISON fuel performance code has undergone significant recent development to expand its TRISO particle fuel performance modeling capabilities. This includes the development of material models, such as elastic, creep, swelling, thermal expansion, thermal conductivity, and fission gas release models. The capability to perform statistical failure analysis on large sets of samples has also been developed, utilizing a Monte Carlo scheme to execute fast-running 1-D spherically symmetric models. Stress adjustments are made in those 1-D models to account for multi-dimensional failure phenomena. Stress correlation functions are extracted from multi-dimensional failure simulation results, such as from a particle with cracked inner pyrolytic carbon (IPyC) and an aspherical particle. This paper provides a detailed description of the models used by BISON for TRISO fuel, along with a set of problems that test these models by (favorably) comparing them both with another code and experimental data. These include simulations of the Advanced Gas Reactor (AGR)-2 and AGR-5/6/7 experiments, with predictions for fuel performance parameters, failure probability, and fission product transport.

© 2021 Elsevier B.V. All rights reserved.

1. Introduction

The tri-structural isotropic (TRISO)-coated fuel particle was originally developed in the late 1950s to support the U.K.'s Dragon reactor. It has been widely used for a number of applications ever since, and is the topic of significant current interest due to being the fuel form employed by multiple Generation-IV reactor concepts such as high-temperature gas-cooled reactors (HTGRs) and fluoride-salt-cooled high-temperature reactors (FHRs). Since TRISO fuel's original development, it has been improved upon in terms of particle design, coating layers, and kernel composition—all of which lead to lower likelihoods of particle failure and better fission product retention. A thorough review of coated particle fuel development is provided in [1].

The TRISO particle is composed of a fissile fuel kernel surrounded by successive coating layers consisting of a porous carbon buffer layer, a dense inner pyrolytic carbon (IPyC) layer, a silicon carbon (SiC) layer, and a dense outer pyrolytic carbon (OPyC) layer.

Recent developments in the U.S. favor the use of uranium oxycarbide (UCO)—a multi-phase mixture of UO_2 , UC, and UC_2 —due to its superior performance [2]. In UO_2 TRISO fuel, CO is produced by reactions between the buffer and excess oxygen liberated by fission. A particular advantage of using UCO for the kernel in TRISO fuel is that its production of CO is negligible, thereby limiting the internal gas pressure that can potentially lead to particle failure. The buffer accommodates the irradiation-induced swelling of the kernel, acts as a reservoir for fission gases in order to limit the internal pressure buildup in the TRISO particle, and protects the IPyC layer by absorbing fission product recoil. The IPyC protects the kernel from chlorine attack during chemical deposition of the SiC and, conversely, protects the SiC from attack by fission products migrating from the kernel; it also serves as a secondary structural layer to alleviate tensile stresses in the SiC and acts as a fission gas barrier. The SiC is both the primary structural layer and primary retention barrier to metallic fission products. It is protected by the OPyC layer during fuel handling. Like the IPyC, the OPyC is a secondary structural layer and fission gas barrier; it also provides a bonding surface to the surrounding matrix material. The TRISO particles are overcoated with resinated graphite powder be-

* Corresponding author.

E-mail address: wen.jiang@inl.gov (W. Jiang).

fore being pressed into a fuel element. The resinated graphite powder transforms into so-called “matrix material” upon pressing and subsequent heat treatments.

Numerous fuel performance codes have been developed for TRISO fuel particle analysis. They include European codes PANAMA [3], STRESS3 [4], ATLAS [5], and STACY [6], and U.S. codes PARFUME [7] and TIMCOAT [8]. Other TRISO fuel performance codes have been developed, in particular in Japan and Korea. A non-exhaustive description of past and existing codes can be found in [9–11]. Unlike the codes specially designed for TRISO, BISON is a nuclear fuel performance tool that is applicable to a variety of fuel forms, i.e., light-water reactor fuel, metallic nuclear fuel, and TRISO fuel [12]. An initial capability of BISON to model TRISO fuel was implemented in 2013 [13]. The code's ability to solve problems of varying dimensionality from 1-D to 3-D was demonstrated at that time. Although BISON previously demonstrated its capability to model a single TRISO fuel particle, significant development has occurred since then. In particular, efforts have focused on predicting particle failure using a statistical treatment to account for the particle-to-particle variations in physical dimensions and fuel properties (layer thickness, density, etc.) arising from the fuel fabrication process. This statistical analysis is also required in order to perform realistic calculations of fission product release from the many particles in a TRISO-fueled reactor. Capability development also occurred in regard to each material present in TRISO fuel particles: the buffer, IPyC, silicon carbide, and OPyC layers, as well as the fuel kernel. For each of these materials, BISON now includes a comprehensive set of thermal, mechanical, and mass diffusion material properties, i.e., elastic, creep, swelling, thermal expansion, thermal conductivity, fission gas release (FGR), and fission product diffusion.

A Monte Carlo scheme is utilized in BISON to calculate the failure probability of TRISO particles. The Monte Carlo simulation computes statistics from many fast-running 1-D analyses. To account for multi-dimensional failure phenomena, effective strengths and stress correlation factors are calculated from high-dimensional models prior to the statistical modeling. They are then used in a 1-D model to determine failure of aspherical particles and particles with cracked IPyC layers. BISON's inherent ability to model a variety of geometries gives it the potential to model TRISO fuel in all situations, without relying on other tools. Another of BISON's advantages is its ability to run analyses in parallel, enabling Monte Carlo samples to be distributed on a cluster using many processors. This capability has proven essential for statistical evaluations of TRISO fuel failure in BISON.

This paper begins by describing the material models newly implemented in BISON for TRISO fuel. The physical models, including governing equations and gap behavior models, are then described. Multiple failure modes are outlined, and the approach to correlate higher-dimensional failure simulation with fast-running 1-D analyses is explained. Three problems are then considered in demonstrating BISON's capability for TRISO failure analysis. The first is a benchmark problem for comparing BISON and PARFUME models of a TRISO UCO fuel particle under representative irradiation conditions. The second problem is a failure analysis of three compacts in the AGR-5/6/7 tests. The final problem considers four compacts in the AGR-2 tests, and their failure probability and fission release fractions are computed. A final section summarizes the conclusions and outlines future work.

2. Model description

2.1. Thermal-mechanical properties

TRISO fuel thermo-mechanical properties for the UCO kernel and coating layers are described in this section. These include elas-

Table 1
Atomic weights of the UCO constituents.

	aw (g/mol)
uranium-235	235.04
uranium-238	238.05
oxygen	16.00
carbon	12.01

tic, creep, swelling, thermal expansion, and thermal conductivity. The validity range of the material models is typically between 0.1 to 3.96×10^{25} n/m² ($E > 0.18$ MeV) for fast neutron fluence and 600 °C to 1300 °C for irradiation temperature. The detailed description of all the models can be found on the BISON's documentation website [14].

2.1.1. UCO fuel kernel

Legacy TRISO fuel development programs have predominantly focused on UO₂ fuel; consequently, most UCO kernel properties currently used in BISON are derived from experimental data on UO₂ and assumed valid for UCO, due to lack of relevant UCO data.

The thermal conductivity of the kernel, k (W/m-K), is given by [7]:

$$k = 0.0132 \exp(0.00188T_C) + \begin{cases} \frac{4040}{464+T_C} & \text{for } T_C < 1650^\circ\text{C} \\ 1.9 & \text{for } T_C \geq 1650^\circ\text{C} \end{cases} \quad (1)$$

where T_C (°C) is the temperature of the kernel.

The specific heat capacity of UCO is calculated from its molar heat capacity [15] and molar mass:

$$c_p = \frac{1}{M} \left(52.1743 + 87.951t_K - 84.2411t_K^2 + 31.542t_K^3 - 2.6334t_K^4 - \frac{0.71391}{t_K^2} \right) \quad (2)$$

where c_p (J/kg-K) is specific heat capacity, $t_K = T_K/1000$ (K) is the reduced temperature, and M (kg/mol) is the molar mass. The molar mass of the kernel, M (kg/mol), is computed for $i = \text{UO}_2$, UC_2 , and UC by:

$$M = \sum_i^N af_i \times aw_i \quad (3)$$

with

$$af = \begin{cases} 0.5OU & \text{for UO}_2 \\ 0.5OU + CU - 1.0 & \text{for UC}_2 \\ 2.0 - (OU + CU) & \text{for UC} \end{cases} \quad (4)$$

and

$$aw = \begin{cases} 0.23504\epsilon + 0.23805(1.0 - \epsilon) + 0.03200 & \text{for UO}_2 \\ 0.23504\epsilon + 0.23805(1.0 - \epsilon) + 0.02402 & \text{for UC}_2 \\ 0.23504\epsilon + 0.23805(1.0 - \epsilon) + 0.01201 & \text{for UC} \end{cases} \quad (5)$$

where ϵ (wt.%) is the initial U-235 enrichment, OU (-) and CU (-) are the initial oxygen-to-uranium and carbon-to-uranium stoichiometries of UCO, af (-) is the atomic fraction, and aw (kg/mol) is the atomic weight. The atomic weights of the UCO constituents are tabulated in Table 1.

The temperature-dependent Young's modulus of the kernel is fitted from plots in [16]:

$$E = 219(1.0 - 1.1 \times 10^{-4}T_C - 2.1 \times 10^{-7}T_C^2 + 3.1 \times 10^{-10}T_C^3 - 1.6 \times 10^{-13}T_C^4) \left(\frac{1.92\rho - 0.92\rho_{th}}{\rho_{th}} \right) \quad (6)$$

where E (GPa) is Young's modulus of the kernel, T_C (°C) is the temperature of the kernel, ρ (g/cm³) is the density of the kernel, and ρ_{th} (g/cm³) is the theoretical density of UCO.

Table 2
Theoretical densities of the UCO mixture components.

	UO ₂	UC	UC ₂
ρ_{th} (g/cm ³)	10.96	13.63	11.28

The theoretical density of the kernel, ρ_{th} (kg/m³), is calculated as:

$$\rho_{th} = \frac{1}{\frac{wf_{UO_2}}{\rho_{th}} + \frac{wf_{UC}}{\rho_{th}} + \frac{wf_{UC_2}}{\rho_{th}}} \quad (7)$$

$$wf = \frac{af \cdot aw}{M} \quad (8)$$

where wf (-) is the weight fraction of each component. The theoretical densities of the UCO mixture components are tabulated in Table 2.

The Poisson's ratio of the kernel, ν (-), is given by:

$$\nu = 1.35 \left(\frac{1.92\rho - 0.92\rho_{th}}{1.66\rho - 0.66\rho_{th}} \right) - 1 \quad (9)$$

where ρ (g/cm³) is the density of the kernel and ρ_{th} (g/cm³) is the theoretical density of UCO.

Kernel swelling occurs throughout irradiation as solid and gaseous atoms released by fission accumulate in the kernel, resulting in a volume increase of the kernel. The volumetric fission-induced swelling model of UCO is taken from the PARFUME code and assumes a constant rate of volume increase due to fission:

$$\Delta\epsilon_{sw} = 0.8\Delta Bu \quad (10)$$

where $\Delta\epsilon_{sw}$ (-) is the volumetric swelling increment of the kernel and ΔBu (fissions/atoms-U) is the burnup increment.

2.1.2. Buffer

The thermal conductivity of the buffer is taken from the PARFUME code:

$$k = \frac{k_{init}k_{theo}\rho_{theo}(\rho_{theo} - \rho_{init})}{k_{theo}\rho_{theo}(\rho_{theo} - \rho) + k_{init}\rho(\rho - \rho_{init})} \quad (11)$$

where k (W/m-K) is the thermal conductivity of the buffer and ρ (kg/m³) is the density of the buffer. The values at initial (ρ_{init}) and theoretical ($\rho_{theo} = 2250$ kg/m³) densities are taken from [17].

The initial thermal conductivity (k_{init}) of the buffer is set to 0.5 W/m-K. It is intended for an initial buffer density of 1000 kg/m³ but is also used for slightly different densities ($\pm 10\%$). Thermal conductivity of the buffer at its theoretical density (k_{theo}) is set to 4.0 W/m-K.

The specific heat capacity of the buffer is given by [18] as 720 J/kg-K.

The isotropic coefficient of thermal expansion of the buffer is given by [7,17]:

$$\alpha = 5 \left(1 + 0.11 \left[\frac{T_C - 400}{700} \right] \right) \quad (12)$$

where T_C (°C) is the temperature of the buffer. The thermal expansion strain is calculated as:

$$\epsilon_{te} = \alpha (T_K - T_{StressFree}) \quad (13)$$

where T_K (K) is the temperature of the buffer and $T_{StressFree}$ (K) is the stress-free temperature.

The Youngs modulus of the buffer, E (GPa), is given by [7,17]:

$$E = 25.5(0.384 + 0.32410^{-3}\rho)(1.0 + 0.23\phi)(1.0 + 1.510^{-4}[T_C - 20]) \quad (14)$$

where ρ (kg/m³) is the density of the buffer, ϕ (10²⁵ n/m², $E > 0.18$ MeV) is the fast neutron fluence, and T_C (°C) is the temperature of the buffer.

Table 3
Polynomial coefficients for the irradiation-induced strain in the buffer material at a density of 1.96 g/cm³.

T (°C)	a_1	a_2	a_3	a_4
1350	-1.42840	-0.19563	0.18991	-0.02591
1032	-1.52390	0.13048	0.06299	-0.01072
600	-1.24080	0.00175	0.08533	-0.01253

The Poisson's ratio of the buffer is set to a constant value of 0.33 [7,17].

The irradiation creep of the buffer and PyC, which leads to their gradual deformation in response to irradiation-induced damage, is directly proportional to the fast neutron fluence. The irradiation creep correlations for the buffer and PyC are taken from [10,13,19]. With K (m²/MPa-n) as the creep constant, σ_i as one of the principal stresses, ν_c as the Poisson's ratio for creep, and Φ (10²⁵ n/m², $E > 0.18$ MeV) as the fast neutron fluence, the creep rate is computed as:

$$\dot{\epsilon}_1 = K[\sigma_1 - \nu_c(\sigma_2 + \sigma_3)]\dot{\Phi} \quad (15)$$

where

$$K = K_0[1 + 2.38(1.9 - \rho)]M_{Irr,Creep} \quad (16)$$

The steady-state creep coefficient, K_0 , is given by [7] as:

$$K_0 = 2.193 \times 10^{-29} - 4.85 \times 10^{-32}T + 4.0147 \times 10^{-35}T^2 \quad (17)$$

where $M_{Irr,Creep} = 2$, ρ is in g/cm³, and T is in °C and bounded by 600 °C and 1350 °C. The irradiation-induced creep coefficient is plotted at different temperatures and densities.

The Poisson's ratio for creep in the buffer is set to a constant value of 0.5 [7,17].

The buffer experiences isotropic irradiation-induced strain, given by [7,17]:

$$\epsilon_{iso} = a_1\phi + a_2\phi^2 + a_3\phi^3 + a_4\phi^4 \quad (18)$$

where ϕ (10²⁵ n/m², $E > 0.18$ MeV) is the fast neutron fluence and a_1 through a_4 are temperature-dependent polynomial coefficients given in Fig. 2. The polynomial coefficients at other temperatures are interpolated from Fig. 2 and tabulated in Table 3.

For other densities, ϵ_{iso} is adjusted by applying a multiplier, given by $\mu = f(\rho)/f(\rho_0 = 1.96)$ where ρ (g/cm³) is the density of the buffer. The isotropic density scaling factor is calculated using the values in Table 4, showing the relationship between isotropic strain and density at an irradiation temperature of 1100 °C and a fast fluence of 3.7×10^{25} n/m² ($E > 0.18$ MeV).

2.1.3. PyC

The thermal conductivity of the PyC layers is 4 W/m-K [7]. The specific heat capacity is 720 J/kg-K [18].

The radial and tangential coefficients of thermal expansion of PyC are given by [7]. The thermal expansion strains, ϵ_i (-), for i = radial, tangential are:

$$\epsilon_i = \alpha_i(T - T_{StressFree}) \quad (19)$$

where α_i is the thermal expansion coefficient (1/K), T (K) is the temperature, and $T_{StressFree}$ (K) is the stress-free temperature.

Thermal expansion coefficients, α_i (10⁻⁶/K), for i = radial, tangential are:

$$\alpha_r = (30 - 37.5R_r) \left(1 + 0.11 \left[\frac{T - 673}{700} \right] \right) \quad (20)$$

and

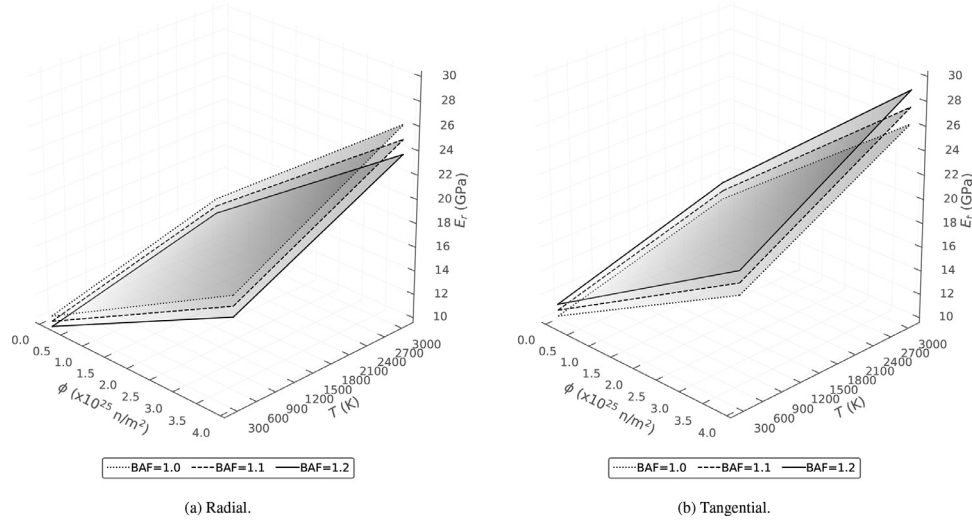
$$\alpha_t = (36[R_t - 1]^2 + 1) \left(1 + 0.11 \left[\frac{T - 673}{700} \right] \right) \quad (21)$$

Table 4Isotropic strain at an irradiation temperature of 1100°C and a fast fluence of 3.7×10^{25} n/m² ($E > 0.18$ MeV).

ρ (g/cm ³)	1.0	1.2	1.4	1.5	1.6	1.8	1.9	1.96	2.0
$f(\rho)$	-16.15	-13.11	-9.98	-8.93	-6.97	-4.42	-3.41	-2.75	-2.33

Table 5BAF vs. fast neutron fluence ($E > 0.18$ MeV).

ϕ ($\times 10^{25}$ n/m ²)	0.0	1.0	2.0	3.0	3.5	4.0	4.5	≥ 5.0
BAF/BAF ₀	1.0000	1.0019	1.0114	1.0219	1.0286	1.0324	1.0362	1.0381

**Fig. 1.** Elastic modulus of PyC as a function of fluence and temperature for various values of baf.

with

$$R_r = \frac{2}{2 + BAF} \quad \text{and} \quad R_t = \frac{1 + BAF}{2 + BAF} \quad (22)$$

where R_i (-) is the orientation parameter in the i -th direction and T (K) is the temperature. The Bacon anisotropy factor (BAF) is a direct measure of the crystallographic anisotropy of pyrolytic carbon coatings deposited on spherical fuel particles. The BAF increases with fast fluence, and the ratio of irradiated to unirradiated baf values is tabulated in Table 5 as a function of fast fluence.

The Youngs modulus of the PyC layers is given by [7,17]. The elastic modulus, E (GPa), is computed as:

$$E = \frac{E_r + E_t}{2} \quad (23)$$

with its radial and tangential components, E_r and E_t , as

$$E_r = 25.5(0.384 + 0.324 \times 10^{-3} \rho)(1.463 - 0.463BAF_0) \times (2.985 - 0.0662L_c)(1 + 0.23\phi)[1 + 0.00015(T - 20)] \quad (24)$$

and

$$E_t = 25.5(0.384 + 0.324 \times 10^{-3} \rho)(0.481 + 0.519BAF_0) \times (2.985 - 0.0662L_c)(1 + 0.23\phi)[1 + 0.00015(T - 20)] \quad (25)$$

where ρ (kg/m³) is the density, BAF_0 (-) is the as-fabricated baf, L_c (Å) is the crystallite diameter, ϕ (10^{25} n/m², $E > 0.18$ MeV) is the fast neutron fluence, and T (°C) is the temperature. The default value of L_c is set at 30Å, so the factor of that term takes a value of 1. The PyC elastic modulus is plotted at different temperatures, fluences, and bafs in Fig. 1.

The Poisson's ratio is set to a constant value of 0.33 [7,17].

The irradiation creep model for the PyC is the same as for the buffer. The Poisson's ratio for creep of the PyC layers is set to a constant value of 0.5.

Under irradiation, PyC shrinks in both the radial and tangential directions. At modest fast neutron fluences, however, it begins to swell in the radial direction. The anisotropic strains, ε_i (-), for i = radial, tangential, and isotropic are given by [7,17]:

$$\varepsilon_i = a_1\phi + a_2\phi^2 + a_3\phi^3 + a_4\phi^4, \quad (26)$$

where ϕ (10^{25} n/m², $E > 0.18$ MeV) is the fast neutron fluence and a_1 through a_4 are BAF- and temperature-dependent polynomial coefficients, listed in Table 6 and Table 7 in terms of the tangential and radial components, respectively. The polynomial coefficients at other temperatures are interpolated or extrapolated from these tables, while at other bafs they are only interpolated from these tables. The PyC radial and tangential strains computed using these coefficients are plotted in Fig. 2(a) and Fig. 2(b), respectively.

Adjustments for PyC with other densities are made by applying an anisotropic scaling factor, ν . This factor is defined as the ratio of the difference between the radial and tangential strain components at a given density to the difference between the radial and tangential strain components at $\rho_0 = 1.96$ g/cm³:

$$\nu = \frac{\varepsilon_r(\rho) - \varepsilon_t(\rho)}{\varepsilon_r(\rho_0) - \varepsilon_t(\rho_0)} \quad (27)$$

The anisotropic scaling factor is calculated using the values in Table 8, which shows the relationship between the difference in the radial and tangential strain components and the density at an irradiation temperature and fast fluence. Thus, the adjusted radial and tangential strains become:

$$\varepsilon_r(\rho) = \mu\varepsilon_{iso}(\rho_0) + \nu[\varepsilon_r(\rho_0) - \varepsilon_{iso}(\rho_0)] \quad (28)$$

$$\varepsilon_t(\rho) = \mu\varepsilon_{iso}(\rho_0) + \nu[\varepsilon_t(\rho_0) - \varepsilon_{iso}(\rho_0)] \quad (29)$$

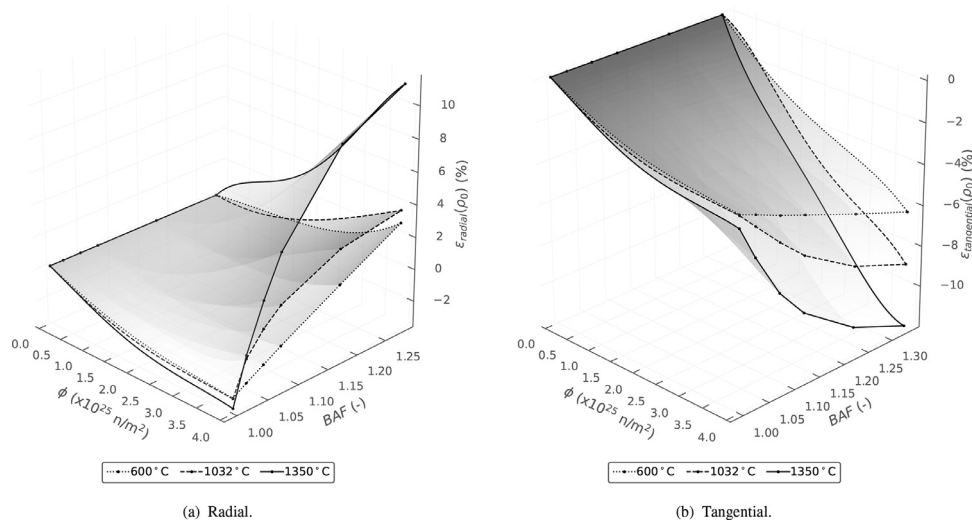


Fig. 2. PyC (a) radial and (b) tangential strain at $\rho_0 = 1.96 \text{ g/cm}^3$ as a function of BAF and fluence for various temperatures.

Table 6

Polynomial coefficients for PyC radial strain components.

	BAF	1.0000	1.0212	1.0488	1.0769	1.1746	1.2787
600°C	a_1	-1.24080	-1.10640	-0.94333	-0.78045	-0.15714	0.40265
	a_2	0.00175	-0.03128	-0.03589	-0.02975	-0.14889	-0.16501
	a_3	0.08533	0.09184	0.08184	0.06655	0.07546	0.03676
	a_4	-0.01253	-0.01220	-0.00958	-0.00626	-0.00293	0.00706
1032°C	a_1	-1.52390	-2.07520	-2.00470	-1.81690	-1.18540	-0.45900
	a_2	0.13048	1.37845	1.30380	1.10850	0.64995	0.51172
	a_3	0.06299	-0.48993	-0.37280	-0.23868	0.01380	-0.03245
	a_4	-0.01072	0.06602	0.04538	0.02484	-0.01284	-0.00142
1350°C	a_1	-1.42840	-1.54330	-1.49640	-0.89522	1.20930	3.71620
	a_2	-0.19563	0.59804	1.16621	0.80331	-0.53861	-2.70420
	a_3	0.18991	-0.09997	-0.30106	-0.09009	0.43114	1.17990
	a_4	-0.02591	0.00978	0.03475	0.00467	-0.05590	-0.13910

Table 7

Polynomial coefficients for PyC tangential strain components.

	BAF	1.0000	1.0303	1.0769	1.1250	1.2258	1.3333
600°C	a_1	-1.24080	-1.38550	-1.46790	-1.64660	-1.84990	-2.19190
	a_2	0.00175	0.05307	-0.02836	0.03928	-0.09358	0.02675
	a_3	0.08533	0.07620	0.12139	0.10067	0.18119	0.15352
	a_4	-0.01253	-0.01245	-0.01948	-0.01764	-0.03036	-0.02972
1032°C	a_1	-1.52390	-1.57590	-1.32200	-1.18700	-0.96963	-0.81239
	a_2	0.13048	0.09019	-0.51928	-0.90635	-1.59110	-2.20760
	a_3	0.06299	0.05306	0.27603	0.41046	0.64689	0.88496
	a_4	-0.01072	-0.00815	-0.03465	-0.05067	-0.07682	-0.10457
1350°C	a_1	-1.42840	-2.24680	-2.82930	-3.25550	-4.44780	-5.67140
	a_2	-0.19563	0.48243	0.76088	0.90423	1.60320	2.41920
	a_3	0.18991	-0.07687	-0.22314	-0.33175	-0.58683	-0.86155
	a_4	-0.02591	0.00464	0.02431	0.04329	0.07458	0.10668

Table 8

Isotropic and anisotropic strain of PyC at an irradiation temperature of 1100°C and a fast fluence of $3.7 \times 10^{25} \text{ n/m}^2$ ($E > 0.18 \text{ MeV}$).

$\rho \text{ (g/cm}^3\text{)}$	1.00	1.20	1.40	1.50	1.60	1.80	1.90	1.96	2.00
$\epsilon_{iso} \text{ (%)}$	-16.15	-13.11	-9.98	-8.93	-6.97	-4.42	-3.41	-2.75	-2.33
$\epsilon_r - \epsilon_t \text{ (%)}$	0.000	0.500	1.100	1.650	2.450	6.305	7.900	9.600	11.100

Table 9
Elastic modulus of SiC as a function of temperature.

T (°C)	25.0	940.0	1215.0	1600.0
E (GPa)	428.0	375.0	340.0	198.0

2.1.4. SiC

The thermal conductivity model for SiC is given by Miller [7]:

$$k = \frac{17885}{T_K} + 2.0 \quad (30)$$

where k (W/m-K) is the thermal conductivity and T_K (K) is the temperature.

The correlation for specific heat capacity, c_p (J/kg-K), is given by [20]:

$$c_p = 925.65 + 0.3772T - 7.9259 \times 10^{-5}T^2 - \frac{3.1946 \times 10^7}{T^2} \quad (31)$$

where T (K) is the temperature.

The thermal expansion coefficient is 4.9×10^{-6} (1/K) [7,17].

The Youngs modulus and Poisson's ratio of SiC is given by [7].

The Youngs modulus (E) is temperature-dependent and given according to Table 9. For values between the tabulated values, linear interpolation is used. For temperatures below 25.0°C, Young's modulus is taken as 428.0 GPa. For temperatures above 1600°C, a value of 198.0 GPa is used.

Poisson's ratio is set to a constant value of 0.13.

2.2. Fission product diffusion

Several mechanisms can be involved in the transport of mobile fission products through the kernel and coating layers of TRISO particles. Such mechanisms could include lattice diffusion, grain boundary diffusion, pore diffusion, nano-cracking, or vapor transport [21]. Furthermore, effects like irradiation-induced trapping and adsorption, thermal decomposition of the coating layers, or chemical attack of the coating layers by other fission products, such as palladium or rare-earth elements, could potentially impact these transport mechanisms. To get by the limited fundamental knowledge of all possible transport mechanisms, Fick's laws of diffusion are used with "effective" diffusivities in order to model fission product transport through TRISO particles.

The effective diffusion coefficient, D (m²/s), is defined in Arrhenius form as:

$$D = D_1 \exp\left(\frac{-Q_1}{RT}\right) + D_2 \exp\left(\frac{-Q_2}{RT}\right) \quad (32)$$

where R is the universal gas constant. Values of D_1 , D_2 , Q_1 , and Q_2 for silver, cesium, and strontium respectively, are given in Table 10 [22,23]. Diffusion coefficients for the kernel are values derived from experimental data on UO₂ fuel. These values are used for the UCO kernel, due to lack of data.

2.3. Fission gas

The release of long-lived fission gases from the kernel is modeled as a two-step process: first, the gas atoms are driven through the grain towards the grain boundary; second, the gas atoms migrate from the grain boundary to the free surface of the fuel, where they are instantaneously released into the free volume of the TRISO particle. The model includes both direct recoil and diffusion to grain boundaries. The release fraction FGR (-), which corresponds to the fraction of the fission gas that is released by the kernel, is given by:

$$FGR = (RF_{recoil} + [1.0 - RF_{recoil}]RF_{Booth})FGP \quad (33)$$

Table 10
Mass diffusion coefficients.

		Kernel (UO ₂ or UCO)	PyC	SiC
Ag	D_1 (m ² /s)	6.7×10^{-9}	5.3×10^{-9}	3.6×10^{-9}
	Q_1 (kJ/mol)	165	154	215
	D_2 (m ² /s)	-	-	-
	Q_2 (kJ/mol)	-	-	-
Cs ^a	D_1 (m ² /s)	5.6×10^{-8}	6.3×10^{-8}	$5.5 \times 10^{-14} e^{(\phi \times 1.1/5)}$
	Q_1 (kJ/mol)	209	222	125
	D_2 (m ² /s)	5.2×10^{-4}	-	1.6×10^{-2}
	Q_2 (kJ/mol)	362	-	514
Sr	D_1 (m ² /s)	2.2×10^{-3}	2.3×10^{-6}	1.2×10^{-9}
	Q_1 (kJ/mol)	488	197	205
	D_2 (m ² /s)	-	-	1.8×10^6
	Q_2 (kJ/mol)	-	-	791

^a Note that ϕ = fast neutron fluence ($\times 10^{25}$ n/m², $E > 0.18$ MeV)

where RF_{recoil} (-) and RF_{Booth} (-) are the release fractions of fission gas in regard to direct recoil and diffusion, respectively, and FGP (mol) is the amount of fission gas produced in the kernel. The model assumes that 100% of the fission gas is released to the void volume.

2.3.1. Direct recoil

Direct kinetic release of fission gases from the kernel to the buffer is accounted for by geometrical considerations and fission fragment ranges derived from compiled experimental data [24]. The fission gas mixture is essentially composed of krypton and xenon, with relative fractions of 18.5 and 81.5% [7] respectively. Hence, the recoil fraction is given by:

$$RF_{recoil} = 0.185RF_{recoil,Kr} + 0.815RF_{recoil,Xe} \quad (34)$$

where $RF_{recoil,Kr}$ (-) and $RF_{recoil,Xe}$ (-) are the respective release fractions of krypton and xenon due to recoil. They depend on the ranges of krypton and xenon in UCO (i.e., r_i for $i = Kr, Xe$) and on the radius of the kernel, r_k (m):

$$RF_{recoil,i} = 0.25 \left(\frac{r_k^3 - [r_k - r_i]^3}{r_k^3} \right) \quad (35)$$

The ranges of krypton and xenon in UCO (i.e., r_i for $i = Kr, Xe$) are obtained from their individual ranges in uranium, carbon, and oxygen:

$$r_i = 10.0 \left(\frac{r_{i,U} + OU r_{i,O} + CU r_{i,C}}{\rho_k [1.0 + OU + CU]} \right) \quad (36)$$

where OU (-) and CU (-) are the initial oxygen-to-uranium and carbon-to-uranium ratios, ρ_k (g/cm³) is the density of the kernel, and the individual ranges are given in Table 11.

2.3.2. Booth model

Diffusive release through kernel grains to the grain boundaries and subsequent transport through the interconnected porosity is estimated by the Booth equivalent sphere diffusion model [25]. The Booth release fraction is given by:

$$RF_{Booth} = 1.0 - \frac{6.0r_{grain}^2}{Dt} \sum_{n=1}^{\infty} \frac{1.0 - \exp\left(\frac{-n^2\pi^2Dt}{r_{grain}^2}\right)}{n^4\pi^4} \quad (37)$$

where r_{grain} (m) is the radius of the diffusing sphere (i.e., the average grain radius), D (m²/s) is the diffusivity of the fission gas in the grain, and t (s) is the diffusion time. The default value of r_{grain} (m) is 10 μ m in BISON.

The UCO model utilizes an effective diffusion coefficient, D_{eff} (m²/s), formulated for UO₂ fuel by [26] as:

$$D_{eff} = \sum_{i=1}^3 D_i \quad (38)$$

Table 11
Range of Kr and Xe in U, C, and O [24].

Fission product Medium Range (mg/cm ²)	Kr uranium 11.7	Kr carbon 3.3	Kr oxygen 3.1	Xe uranium 8.3	Xe carbon 2.3	Xe oxygen 2.2
--	-----------------------	---------------------	---------------------	----------------------	---------------------	---------------------

where D_1 , D_2 , and D_3 are the diffusion coefficients of the mechanisms controlling diffusion at different temperature ranges.

- At the highest temperatures, diffusion proceeds through the cation lattice by means of thermally activated vacancies:

$$D_1 = 7.6 \times 10^{-10} \exp\left(-\frac{35225}{T_K}\right) \quad (39)$$

where T_K (K) is the temperature of the kernel.

- At intermediate temperatures, diffusion is driven by means of vacancies produced by the irradiation process:

$$D_2 = s^2 j_v \left(\frac{K'}{Z j_v}\right)^{0.5} \quad (40)$$

where s (m) is the atomic jump distance, j_v (s^{-1}) is the cation vacancy jump rate, K' (s^{-1}) is the rate of defect production per atom, and Z (-) is the number of sites around a point defect from which recombination is inevitable. They are given by:

$$j_v = 10^{13} \exp\left(-\frac{27778}{T_K}\right) \quad (41)$$

$$K' = \frac{KB_u}{t} \quad (42)$$

$$s = 3.0 \times 10^{-10} \quad \text{and} \quad Z = 2 \quad (43)$$

where K (10^4 defects/fission) is the damage rate and B_u in %FIMA (fissions per initial metal atom) is the burnup.

- Finally, at lower temperatures, a term proportional to the fission rate density, f''' (fission/ m^3 -s), is used to agree with experimental results reported by [26]:

$$D_3 = 2.0 \times 10^{-40} f''' \quad (44)$$

2.3.3. Fission gas production

The amount of fission gas produced by the kernel, F_{GP} (mol), during a time interval, Δt (s), is calculated as:

$$F_{GP} = \frac{\Gamma_{FG} f''' V_k \Delta t}{N_{avo}} \quad (45)$$

where Γ_{FG} (-) is the combined fractional fission yield of gaseous fission product atoms (assumed to be krypton and xenon) per fission, V_k (m^3) is the volume of the kernel, and N_{avo} (6.022×10^{23} at/mol) is Avogadro's number.

2.3.4. Fission yields

Fission yields, Γ (atoms/fission), for silver, cesium, strontium, and the combination of krypton and xenon are given below.

- For silver:

$$\Gamma_{Ag} = \begin{cases} 1.31625 \times 10^{-3} b^{0.55734} & \text{for } e < 17.5 \\ 8.24492 \times 10^{-4} b^{0.53853} & \text{for } e \geq 17.5 \end{cases} \quad (46)$$

with $b = \max(1.0, Bu)$.

- For cesium:

$$\Gamma_{Cs} = \begin{cases} 0.14 & \text{for } e < 17.5 \\ 0.16 & \text{for } e \geq 17.5 \end{cases} \quad (47)$$

- For strontium:

$$\Gamma_{Sr} = \begin{cases} 0.11754 b^{-0.21762} & \text{for } e < 17.5 \\ 0.11819 b^{-0.15778} & \text{for } e \geq 17.5 \end{cases} \quad (48)$$

with $b = \max(0.6, Bu)$.

- For krypton and xenon, the elements are assumed to comprise the gaseous fission yield, Γ_{FG} , (taken from the PARFUME code):

$$\Gamma_{Kr+Xe} = \Gamma_{FG} = 0.297 \quad (49)$$

where B_u (%FIMA) is the burnup and e (%) is the ^{235}U enrichment.

3. Physical models

BISON [27] is a finite element based fuel performance code developed at Idaho National Laboratory (INL) to simulate the performance of a variety of nuclear fuel forms. BISON is built on the open-source MOOSE multiphysics framework [28], which provides core functionality needed to solve coupled physics field equations with the finite element method using an implicit scheme.

3.1. Governing equations

TRISO simulation is based on the three partial differential equations generally at the center of all fuel performance modeling activities: energy balance (Eq. 50), conservation of momentum or static equilibrium (Eq. 52), and mass diffusion (Eq. 51).

The heat equation is expressed as:

$$\rho C_p \frac{\partial T}{\partial t} + \nabla \cdot \mathbf{q} - E_f \dot{F} = 0 \quad (50)$$

where T is temperature, the primary unknown. ρ and C_p are density and specific heat respectively, and E_f is the energy released per fission. \dot{F} is the volumetric fission rate.

Fission product species conservation, or mass diffusion, is given by:

$$\frac{\partial C}{\partial t} + \nabla \cdot \mathbf{J} + \lambda C - S = 0 \quad (51)$$

where C is concentration, the primary variable, and λ and S are the radioactive decay constant and source rate of a given species respectively. The radioactive decay term is not considered in this work.

Conservation of momentum, or static equilibrium, is prescribed using Cauchy's equation:

$$\nabla \cdot \boldsymbol{\sigma} + \rho \mathbf{f} = 0 \quad (52)$$

where $\boldsymbol{\sigma}$ is the Cauchy stress tensor and \mathbf{f} is the body force per unit mass (e.g., gravity). In this work, the body force term is neglected. A general constitutive law for Cauchy stress is given for small strains as:

$$\boldsymbol{\sigma} = \mathbb{C} : (\boldsymbol{\varepsilon} - \boldsymbol{\varepsilon}_{\text{creep}} - \boldsymbol{\varepsilon}_{\text{thermal_expansion}} - \boldsymbol{\varepsilon}_{\text{irradiation_strain}}) \quad (53)$$

where \mathbb{C} is the elasticity tensor, $\boldsymbol{\varepsilon}$ is the total strain, and the last three terms are the irradiation creep strain, thermal expansion eigenstrain, and irradiation-induced eigenstrain, respectively. The creep strain is calculated implicitly utilizing a radial return algorithm. Finite strain introduces more complexity and, for the sake of brevity, is not covered here. The nonlinear finite strain kinematics are solved in an incremental form, and a detailed description is provided in [27].

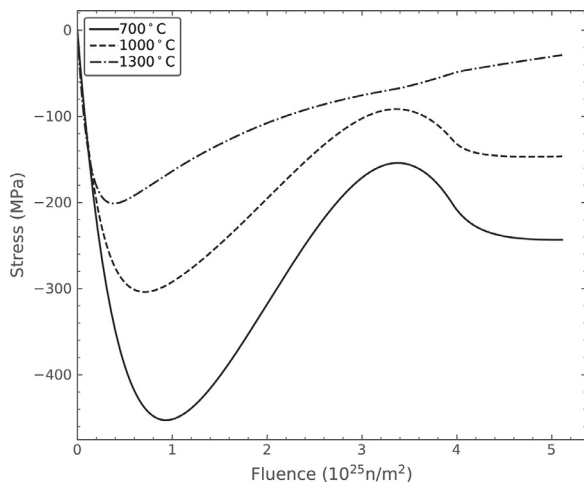


Fig. 3. Evolution of tangential stress with burnup at the inner surface of the SiC layer.

3.2. Gap behavior

As the buffer layer shrinks under irradiation, a gap can form between the buffer and IPyC layer. Heat produced in the kernel is transferred to the outer coating layers through the buffer-IPyC gap via a gap conductance model. Similarly, fission products generated in the kernel are transferred to the outer coating layers through the gap via a mass conductance model. Although BISON can model mechanical contact between the buffer and IPyC surfaces, it is not used in practice for TRISO modeling because the gap usually remains open during irradiation. A detailed description of the gap behavior model can be found in [13].

4. Failure analysis

The ability of the fuel to contain fission products is largely dictated by the quality of the manufacturing process, since most of the fission product release is expected to occur due to coating layer failure in a small number of particles at the locations of defects. To account for statistical variation in physical dimensions and material properties from particle to particle, a Monte Carlo scheme is utilized to compute failure probability for a statistically sampled batch of particles. This enables realistic calculations of fission product release from the many particles in a TRISO-fueled reactor.

4.1. Failure modes

Several potential failure mechanisms for TRISO fuel, outlined in the sections below, are considered in the current work. Other failure modes in addition to those discussed here are both possible and potentially important, and techniques to consider them are in active development.

4.1.1. Pressure vessel failure

Early on during irradiation, pyrolytic carbon layers shrink, compressing the SiC layer. As irradiation progresses, the creep of the pyrolytic carbon layers tends to relax some of this compressive stress. In addition, the buildup of fission gas pressure tends to put all the coating layers in tension. Fig. 3 shows the evolution of tangential stress with burnup at the inner surface of the SiC layer under three temperature conditions. This stress value is important, as it is used to determine whether a particle fails. Since CO production in a UCO kernel is relatively small, gas pressure is usually not high enough to make the tangential stress in the SiC layer become

tensile. Therefore, pressure vessel failure is not likely to occur for an intact TRISO UCO kernel at low and intermediate temperatures.

4.1.2. Cracking of the IPyC

During irradiation, shrinkage of the pyrolytic carbon layers causes significant tensile stress in those layers. If the stress exceeds the tensile strength of the material, a radial crack can form in a pyrolytic carbon layer. Such a crack leads to high local tensile stress in the SiC layer adjacent to that cracked pyrolytic carbon layer, potentially causing failure of the SiC layer and, therefore, of the particle. In Figure 4(a), a discrete crack in the IPyC layer is represented in the finite element model using the extended finite element method [29]. As shown in Figure 4(b), the stress in the SiC layer near the crack tip is elevated significantly due to the development of cracking in the IPyC layer.

4.1.3. Pressure vessel failure of an aspherical particle

A single flat facet on one side of the particle created during fabrication is a common cause of aspherical behavior in particle fuel. The degree of asphericity for a particle is measured by the aspect ratio. During irradiation, the faceted portion of the particle acts as a flat plate that retains the internal gas pressure. If the pressure builds up high enough, this results in a local region of tensile stress in the central portion of the plate, potentially contributing to particle failure. In the scenario shown in Fig. 5(b), the tangential stresses in the SiC layer remain compressive through the end of irradiation because the CO production is limited in UCO fuel.

4.2. Weibull failure theory

A Weibull failure criterion is used to determine vessel failure for the IPyC layer and SiC layer. The maximum stress, σ_c , is compared to a strength sampled from a Weibull distribution having mean strength σ_{ms} and Weibull modulus m . Failure occurs when σ_c exceeds the sampled strength. The cumulative distribution function for the Weibull distribution is given as:

$$P = 1 - \exp\left(-\left(\frac{\sigma_c}{\sigma_{ms}}\right)^m\right) \quad (54)$$

The effective mean strength σ_{ms} is given as:

$$\sigma_{ms} = \frac{\sigma_0}{I_n^{\frac{1}{m}}} \quad (55)$$

where σ_0 is the characteristic strength. The integral, I_n , is a normalized integration of the stress distribution using the principle of independent action (PIA) model as follows:

$$I_n = \frac{\int_V (\sigma_1^m + \sigma_2^m + \sigma_3^m) dV}{\sigma_c^m} \quad (56)$$

where σ_c is the maximum value calculated for a principal stress anywhere in the volume and σ_1 , σ_2 , and σ_3 are three principal stresses. Negative principal stresses are not included in this integral because the compressive stresses do not contribute to fracture.

The Weibull modulus (m) and characteristic strength (σ_0) for the SiC are held constant throughout irradiation and are given as:

$$m = 6 \text{ and } \sigma_0 = 9.64 \times 10^6 \text{ Pa-m}^{3/6} \quad (57)$$

The Weibull modulus for the PyC is assumed to be 9.5, which corresponds to a density of 1.9 g/cm³.

The Weibull characteristic strength of the PyC [7,17] is a function of anisotropy and determined from the following equation for room temperature:

$$\sigma_0 = 10^6 \times (154.46X^2 - 141.1X) \quad (58)$$

where X is a fitting parameter with a default value of 1.02. The characteristic strength has units of Pa-m^{3/9.5} when the Weibull modulus is 9.5.

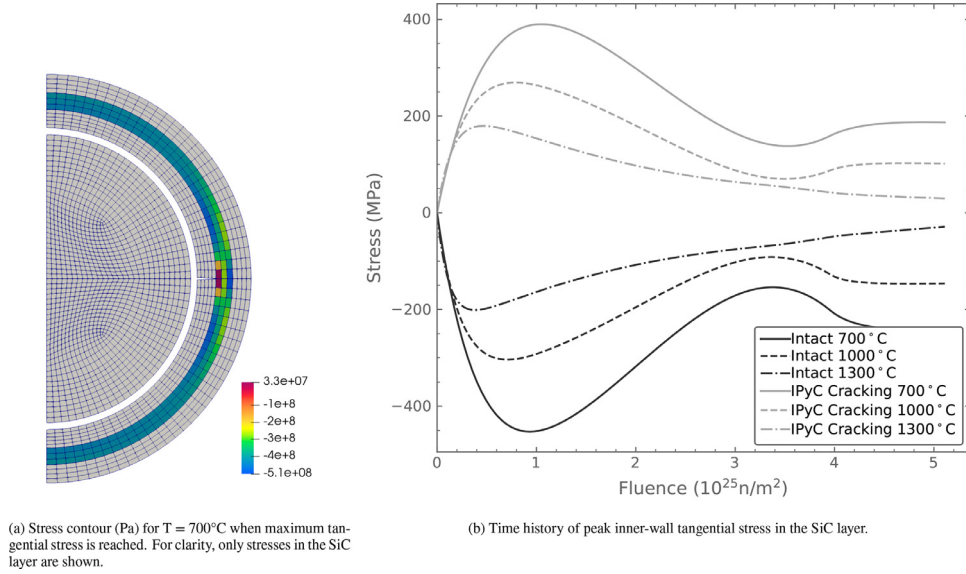


Fig. 4. 2-D axisymmetric model of postulated cracking of the IPyC layer, and time-dependent results for that model.

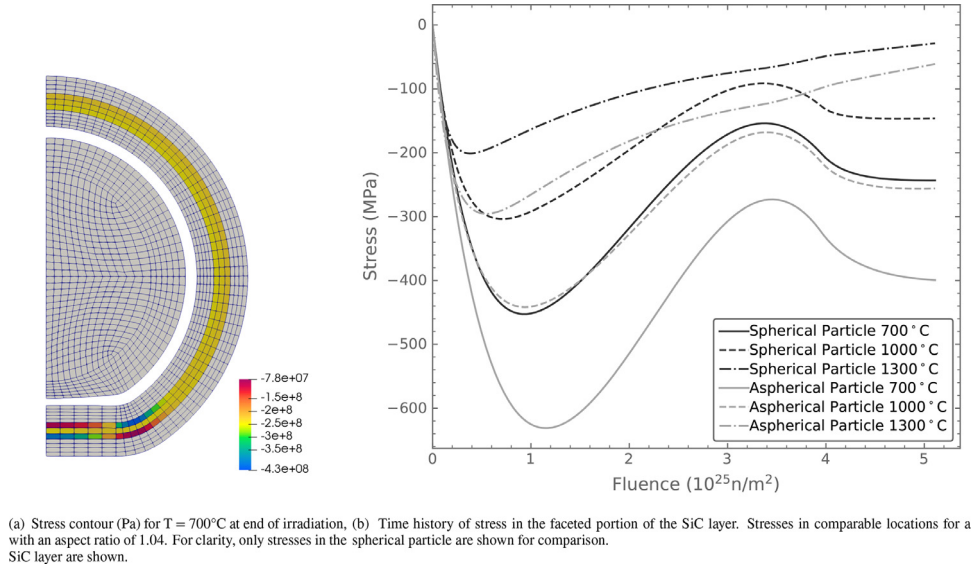


Fig. 5. 2-D axisymmetric model of an aspherical particle, and time-dependent results for that model.

To account for other temperatures and non-zero fluence, Eq. 58 is multiplied by a factor as follows:

$$\text{factor} = [(1 + 0.23\phi)(1 + 0.00015T)]^{1/2} \quad (59)$$

where ϕ (10^{25} n/m^2 , $E > 0.18 \text{ MeV}$) is the fast neutron fluence and T ($^\circ\text{C}$) is the temperature.

4.3. High-fidelity analysis of stress concentrations

For computational efficiency, it is important that each Monte Carlo sample is evaluated using a 1-D model. However, stress concentrations due to the presence of phenomena such as cracking must be characterized using a higher-dimensional model. To account for these multi-dimensional phenomena within a 1-D TRISO model, a high-dimensional failure simulation is performed to obtain the mean effective strength and stress correlation function, based on a multi-dimensional stress distribution. Those values are used in the 1-D model to make adjustments to the stress in failure determination.

4.3.1. Stress correlation for IPyC cracking

The maximum tangential stress histories in the SiC layer for both a cracked particle (near the crack tip) and an intact particle are shown in Fig. 6. The maximum SiC stress in a cracked particle is approximated as:

$$\sigma_{\text{IPyC-cracking}} = \frac{\bar{\sigma}_{2D}}{\bar{\sigma}_{1D}} \sigma_{1D} \quad (60)$$

where $\bar{\sigma}_{2D}$ and $\bar{\sigma}_{1D}$ are the maximum stress calculated in the 2-D and 1-D analyses at the mean values for a specified batch of particles, respectively. Upon varying statistical parameters, the maximum stress in the SiC layer is determined from the 1-D finite element solution for σ_{1D} . The mean strength of the 2-D model, as evaluated at the maximum tangential stress state, will be used for 1-D analysis.

4.3.2. Stress correlation for an aspherical particle

The tangential stress histories for representative faceted and spherical fuel particles are shown in Fig. 7. In evaluating the effect of asphericity, a second term is added to correctly estimate

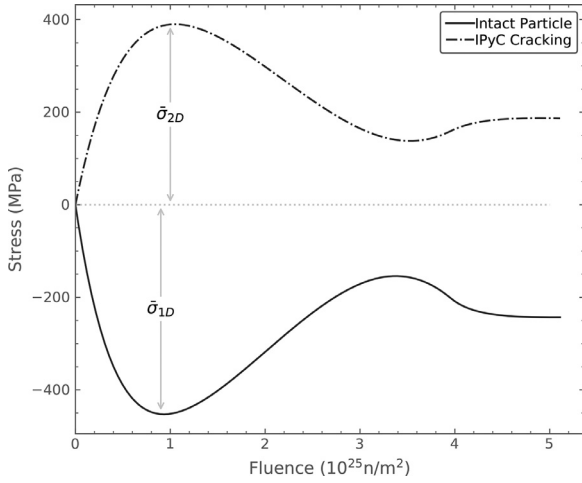


Fig. 6. Time histories of maximum tangential stress in the SiC layer for a 2-D model of a particle with a cracked IPyC layer, compared with a 1-D model of an intact particle. These are used to develop the stress correlation for IPyC cracking.

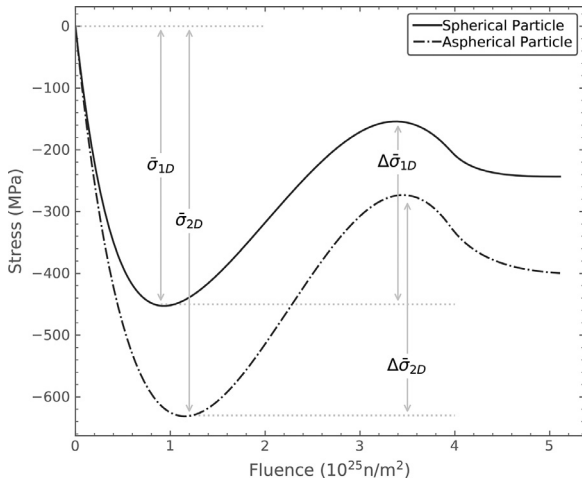


Fig. 7. Time histories of the maximum tangential stress in the SiC layer for a 2-D model of an aspherical particle with an aspect ratio of 1.04, compared to a 1-D model of a spherical particle. These are used to develop the stress correlation for an aspherical particle.

the maximum stress, σ_c , for an aspherical particle:

$$\sigma_{\text{aspherical-particle}} = \frac{\bar{\sigma}_{2D}}{\bar{\sigma}_{1D}} \sigma_{1D-\text{min}} + \frac{\Delta \bar{\sigma}_{2D}}{\Delta \bar{\sigma}_{1D}} \Delta \sigma_{1D} \quad (61)$$

where $\Delta \bar{\sigma}_{2D}$, $\Delta \bar{\sigma}_{1D}$, and $\Delta \sigma_{1D-\text{min}}$ are changes in the stresses $\bar{\sigma}_{2D}$, $\bar{\sigma}_{1D}$, and $\sigma_{1D-\text{min}}$, going from the minimum to the end of irradiation. If a second extremum (or maximum) occurs before the end of irradiation, $\Delta \bar{\sigma}_{2D}$, $\Delta \bar{\sigma}_{1D}$, and $\Delta \sigma_{1D}$ are taken as changes in these stresses, going from minimum to maximum. The additional term is needed because pressure vessel failure of aspherical particles typically occurs after the minimum stress is reached, when shrinkage effects from the PyC are decreasing and the inner pressure keeps accumulating. The mean effective strength of the 2-D model evaluated at the end of irradiation will be used in 1-D analysis.

4.4. Monte Carlo scheme

4.4.1. Methodology

Fig. 8 depicts the methodology used to calculate the failure probability of a population of TRISO particles. This methodology relies on a Monte Carlo scheme in which each particle analyzed is a realization of a set of statistically sampled parameters from the

distributions of as-fabricated fuel characteristics (e.g., dimensions, densities, etc.) that can be found among the particles in a fuel element. For each sample, BISON runs a 1-D model of a TRISO particle over the irradiation history. For particles with localized flaws (i.e., aspherical particles and particles with cracked IPyC), an adjustment of the maximum stress and effective mean strength will be made, as described in Section 4.3.

At each time step, the following failure mechanisms are checked:

- Pressure vessel failure of a spherical or aspherical particle: Failure occurs when the maximum tangential tensile stress of the SiC layer due to internal gas pressure is greater than the strength of the SiC.
- SiC failure due to IPyC cracking: Cracking of the IPyC occurs when the maximum tangential tensile stress in the IPyC layer is greater than its strength. A cracked IPyC changes stress from compression to tensile in the SiC layer. SiC failure occurs when the maximum tangential tensile stress of the SiC layer due to IPyC cracking is greater than its strength.

The methodology laid out in Fig. 8 can also be used to simulate fission product diffusion for a collection of fuel particles. The fission product diffusion calculations combine the release fractions (release normalized to calculated inventory) of all TRISO particles in the Monte Carlo sample. Coating layers determined to be failed are assigned a large diffusivity (e.g., $10^{-6} \text{ m}^2/\text{s}$) to model the loss of retention power of that layer. Release is calculated via Fickian diffusion, while inventory is obtained from fission rate density and fission yields.

4.4.2. MOOSE Stochastic tools module

BISON is built on the open-source MOOSE multiphysics simulation framework [28]. In addition to providing a computational framework for solving partial differential equations, MOOSE also supports stochastic analysis for MOOSE-based applications, including BISON, through the “Stochastic Tools” module. MOOSE has a built-in system known as “MultiApps” for running a set of sub-simulations from a single controlling simulation. This was originally developed to connect physics models provided by another set of finite element models to a main simulation. For example, it was used to tie the results of fuel performance models of individual fuel rods to a model of the physics of a full light-water reactor core [30]. The MultiApps system is designed to take full advantage of parallel computing resources by flexibly distributing the sub-simulation models out across the full set of processors available.

More recently, MOOSE’s MultiApps system was utilized by the Stochastic Tools module to perform Monte Carlo sampling. Because it uses MOOSE’s built-in MultiApps system for memory-based data transfer and management of parallel computing resources, it is extremely efficient and scalable. Although a number of other statistical tools are available and could be used to perform sampling for BISON, the computational overhead caused by data input/output for each sample for these external tools is significant compared to the computation time for an efficient 1-D model. In contrast, MOOSE’s built-in Monte Carlo sampling incurs very minimal computational overhead for data transfers, making it possible to run a very large number of Monte Carlo samples. In addition, all the samples can be executed on a cluster in parallel, thereby taking advantage of its multiple processors. Because the probability of failure for TRISO particles is generally quite low, a large number of samples is required to accurately compute failure probability. Hence, this capability is essential for the statistical evaluation of failure probability for TRISO particles in BISON.

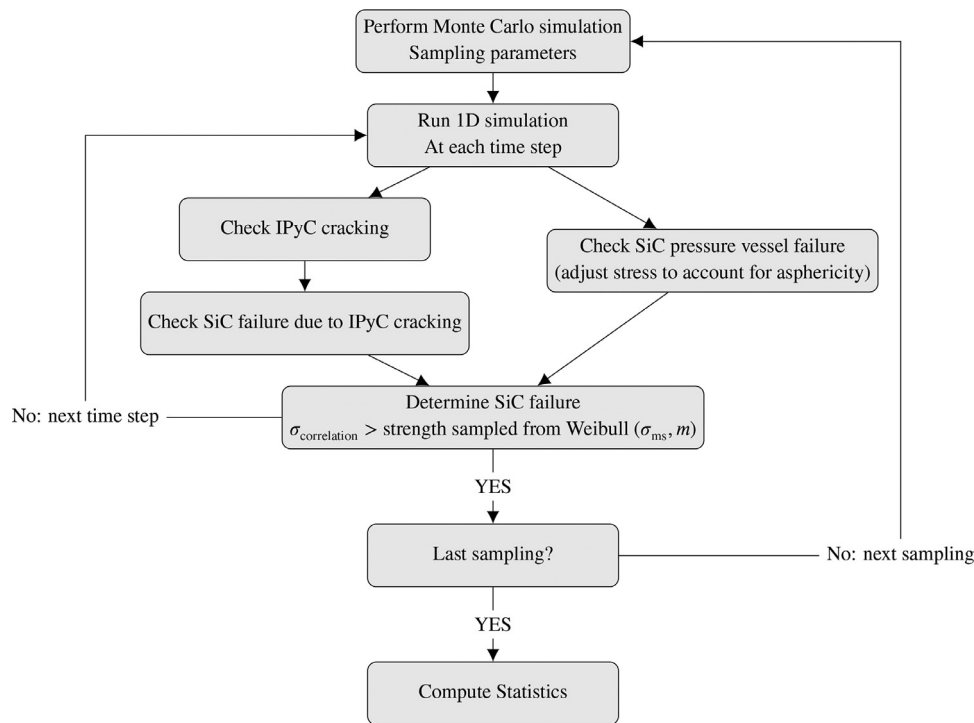


Fig. 8. Monte Carlo scheme employed by BISON for calculating the failure probability of TRISO particles.

Table 12
Irradiation conditions for benchmark problems.

Conditions	EFPD	Burnup (%FIMA)	Fast fluence ($\times 10^{25}$ n/m ²), $E > 0.18$ MeV	Irradiation temperature (°C)
1	500	13.5	5	700
2	500	13.5	5	1000
3	500	13.5	5	1300

5. Demonstration problems

In a previous code verification exercise [13], BISON was applied to 13 of the 16 fuel performance benchmark cases identified as part of an IAEA Coordinated Research Program on HTGR fuel technology [31]. BISON comparisons to either analytical or numerical solutions from other codes in that exercise were very good. In this section, several additional numerical examples are considered in order to demonstrate BISON's new capability of performing particle failure analysis on particle populations. These include benchmarking comparisons against PARFUME and simulations of experiments conducted as part of the U.S. Department of Energy (DOE)'s AGR program.

5.1. Benchmarking of BISON against PARFUME

Here, BISON is compared with PARFUME in terms of a TRISO UCO fuel particle under representative irradiation conditions. This benchmarking exercise consists of first comparing the time histories of multiple quantities of interest for an intact particle, then comparing the probability of failure of that particle under the same conditions. These conditions are summarized in Table 12. Temperatures of 700°C, 1000°C, and 1300°C were chosen so as to fall within the validity range of the material properties. The fuel parameters given in Table 13 are based on the AGR-5/6/7 fuel specification. A brief description of AGR-5/6/7 experiments is provided in the next section.

Table 13
Fuel parameters in benchmark problems.

Category	Parameter	Nominal values
Fuel characteristics	²³⁵ U enrichment (wt%)	15.5
	Carbon/uranium (atomic ratio)	0.4
	Oxygen/uranium (atomic ratio)	1.5
Particle geometry	Kernel diameter (μm)	425
	Buffer thickness (μm)	100
	IPyC/OPyC thickness (μm)	40
	SiC thickness (μm)	35
Fuel properties	Kernel density (g/cm ³)	11.0
	Kernel theoretical density (g/cm ³)	11.4
	Buffer density (g/cm ³)	1.05
	Buffer theoretical density (g/cm ³)	2.25
	IPyC density (g/cm ³)	1.90
	OPyC density (g/cm ³)	1.90
	IPyC/OPyC BAF	1.05

For each of the three conditions of Table 12, the tangential stress histories at the inner and outer surfaces of each layer are plotted in Fig. 9. The tangential stresses are tensile in the IPyC and OPyC layer, and compressive in the SiC layer. The extrema of tensile stress in both PyC layers and compressive stress in the SiC layer decrease with increased temperature, due to irradiation creep. The internal pressure that results in increasing tensile stress in the SiC layer is caused by fission gas buildup. The amount of fission gas in the gap is plotted in Fig. 9d. All those results show good agreement between BISON and PARFUME.

The statistical distributions of particle dimensions and material properties used in the failure probability analysis are listed in Table 14. The stress correlation functions and effective mean strength are pre-computed for each condition, and their values are listed in Table 15. BISON and PARFUME are both used to compute the probability of IPyC layer cracking and SiC layer failure using these distributions. Both codes use the same stress correlation factors and effective mean strength computed by BISON and listed in Table 15. Results are reported in Table 16 and, though not iden-

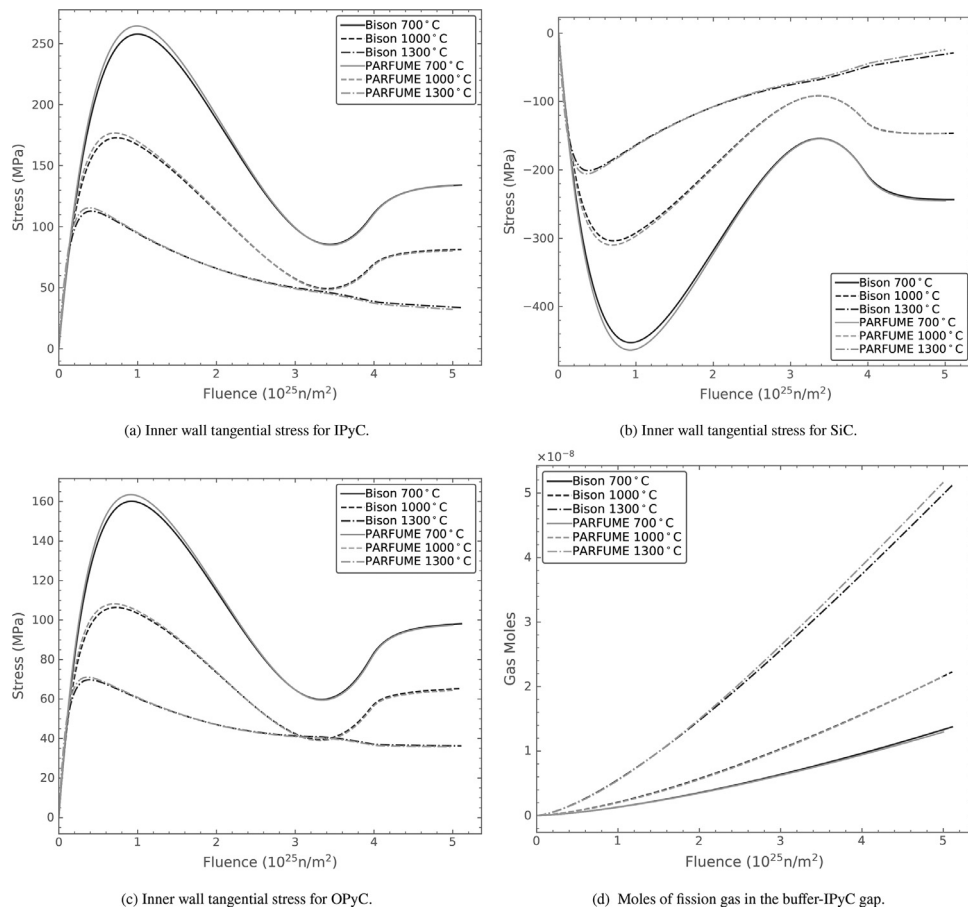


Fig. 9. Time histories of various quantities of interest in the BISON/PARFUME benchmark comparison.

Table 14
Statistical variation of fuel parameters for benchmark problems.

Category	Parameter	Nominal values \pm Standard Deviation
Particle geometry	Kernel diameter (μm)	425 \pm 10
	Buffer thickness (μm)	100 \pm 10
	IPyC/OPyC thickness (μm)	40 \pm 3
	SiC thickness (μm)	35 \pm 2
	Particle asphericity (SiC aspect ratio)	1.04
Fuel properties	IPyC density (g/cm^3)	1.90 \pm 0.02
	OPyC density (g/cm^3)	1.90 \pm 0.02
	IPyC/OPyC BAF	1.05 \pm 0.005

Table 15
Stress correlation factors and effective mean strength for benchmark problems.

Conditions	Intact	IPyC cracking		Asphericity		
	$\sigma_{\text{ms}}(\text{MPa})$	$\sigma_{\text{ms}}(\text{MPa})$	$\frac{\sigma_{20}}{\sigma_{10}}$	$\sigma_{\text{ms}}(\text{MPa})$	$\frac{\sigma_{20}}{\sigma_{10}}$	$\frac{\Delta\sigma_{20}}{\Delta\sigma_{10}}$
1	711	1198	-0.87	993	1.41	1.22
2	719	1198	-0.97	1041	1.59	1.41
3	719	1198	-0.97	1095	1.60	1.48

Table 16
Failure probability for benchmark problems.

Conditions	BISON		PARFUME	
	IPyC cracking	SiC failure	IPyC cracking	SiC failure
1	9.11×10^{-1}	0.75×10^{-3}	8.94×10^{-1}	1.03×10^{-3}
2	7.10×10^{-2}	6.10×10^{-6}	5.48×10^{-2}	7.80×10^{-6}
3	0.80×10^{-3}	1.00×10^{-8}	1.16×10^{-3}	1.64×10^{-8}

Table 17
Irradiation conditions for AGR-5/6/7 Compacts 5-1-3, 5-2-3, and 5-6-1.

Compact	EPFD	Burnup (%FIMA)	Fast fluence ($\times 10^{25} \text{ n/m}^2$)	Irradiation temperature ($^{\circ}\text{C}$)
5-1-3	510	12.67	4.54	803
5-2-3	510	12.17	4.19	812
5-6-1	510	8.24	2.25	696

tical, show reasonable agreement. The slight discrepancy in computed failure probability is possibly due to different numerical approaches and implementation in the two codes. It is worthwhile to mention that the SiC failure probability of condition 3 is so low that the number of samples needed for Monte Carlo simulation is beyond BISON's current practical limit of about 100 million samples. Development of a more efficient approach to handle cases with low failure probability is planned to address this.

5.2. AGR-5/6/7 irradiation test predictions

DOE's AGR program planned a series of irradiation experiments on TRISO fuel. The AGR-5/6/7 experiments test TRISO particles with high-assay low enriched UCO fuel. The AGR-5/6/7 test train houses five capsules, with each capsule containing compacts filled with TRISO particles. The TRISO particle geometry and material properties are the same as those listed in Table 13 and Table 14. The details of these experiments can be found in [32].

Failure probability calculations are performed using BISON on three compacts in Capsule 5. Their irradiation conditions are listed in Table 17. For these compacts, the inner-wall tangential stresses

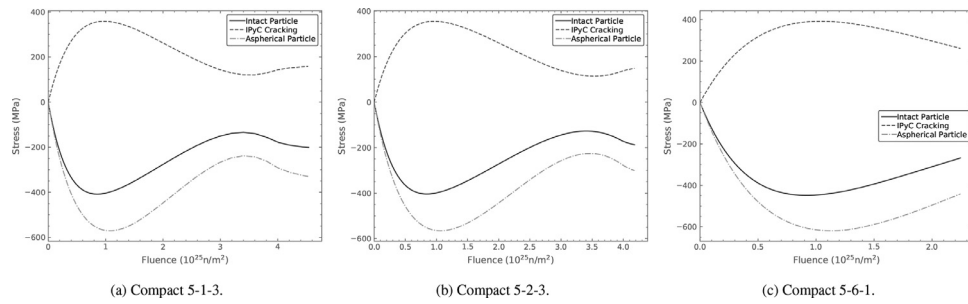


Fig. 10. Evolution of inner-wall tangential stress in SiC for an intact particle, a particle with IPyC cracking, and an aspherical particle in AGR-5/6/7 Compacts 5-1-3, 5-2-3, and 5-6-1.

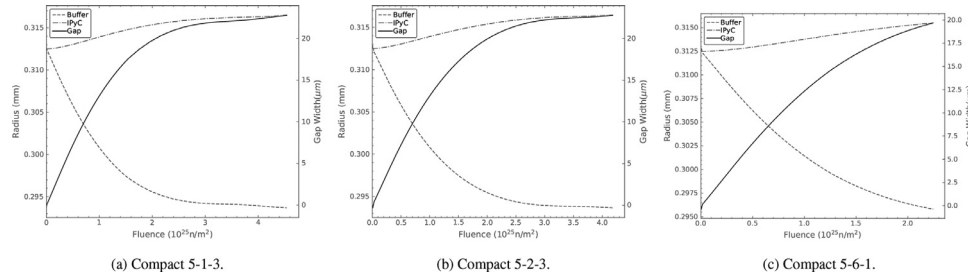


Fig. 11. Evolution of buffer outer and IPyC inner radii for AGR-5/6/7 Compacts 5-1-3, 5-2-3, and 5-6-1. The gap is computed as the difference between these radii.

Table 18

Stress correlation factors and effective mean strength for AGR-5/6/7 Compacts 5-1-3, 5-2-3, and 5-6-1.

Compact	Intact	IPyC cracking		Asphericity		
	σ_{ms} (MPa)	σ_{ms} (MPa)	$\frac{\bar{\sigma}_{IPyC}}{\bar{\sigma}_{SiC}}$	σ_{ms} (MPa)	$\frac{\bar{\sigma}_{SiC}}{\bar{\sigma}_{IPyC}}$	$\frac{\Delta\bar{\sigma}_{SiC}}{\bar{\sigma}_{IPyC}}$
5-1-3	710	1199	-0.96	988	1.53	1.33
5-2-3	711	1199	-0.96	998	1.53	1.34
5-6-1	708	1199	-0.96	1034	1.51	1.06

Table 19

Failure probability for AGR-5/6/7 Compacts 5-1-3, 5-2-3, and 5-6-1.

Compact	IPyC cracking	SiC failure
5-1-3	7.45×10^{-1}	7.34×10^{-4}
5-2-3	6.55×10^{-1}	4.90×10^{-4}
5-6-1	9.15×10^{-1}	1.31×10^{-3}

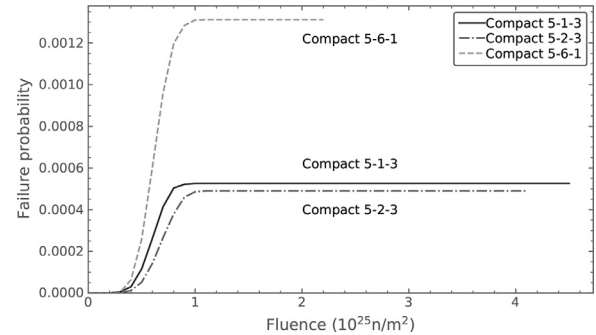


Fig. 12. Evolution of SiC failure probability computed by BISON for AGR-5/6/7 Compacts 5-1-3, 5-2-3, and 5-6-1.

in the SiC layer of an intact particle, a particle with IPyC cracking, and an aspherical particle are plotted in Fig. 10. The evolution of the buffer outer and IPyC inner radii and the buffer-IPyC gap with fluence are plotted in Fig. 11. Since the buffer-IPyC gap contributes a significant percentage of the thermal resistance in a TRISO particle, increasing gap size is expected to cause increased temperature in the fuel kernel. Both Fig. 10 and Fig. 11 are obtained for particles at their nominal fuel geometry and property values shown in Table 13 and Table 14. The aspect ratio for the aspherical particle is 1.04.

The stress correlation factors and effective mean strength for each compact are provided in Table 18. Table 19 summarizes the failure probabilities of IPyC cracking and SiC failure. The evolution of SiC failure probability is plotted in Fig. 12. The SiC failures of all three compacts in Capsule 5 are due to IPyC cracking, which causes a localized tensile stress in the SiC layer. Compact 5-6-1 has the highest SiC failure probability because it was irradiated at lower temperature. The lower temperature causes less creep of the IPyC

layer to offset the shrinkage and relieve tensile stress, thus increasing the probability of IPyC cracking.

The normalized histograms of statistically varying parameters for failed particles in Compact 5-1-3 are shown in Fig. 13. Fitted probability density functions (PDFs) for these parameters are shown for each parameter, along with a PDF for the same parameter for the full set of samples. As seen from those plots, there are significant differences between these PDFs for the IPyC thickness and SiC thickness parameters, indicating that these parameters significantly affect failure. Differences between the PDFs for other parameters are relatively small, indicating that those parameters have little effect on particle failure. The mean value of the SiC thickness for the failed particles is smaller than that for all the particles. This implies that a thinner SiC layer leads to more failed particles. This is intuitive, since it would lead to higher tangential stress in that layer. Conversely, the mean value of the IPyC thickness for failed particles is larger than that for the full set of samples. This indicates that, as the IPyC thickness increases, particle failure becomes more likely. This is because, as the IPyC layer thickens, the irradiation-induced shrinkage increases and, subsequently, height-

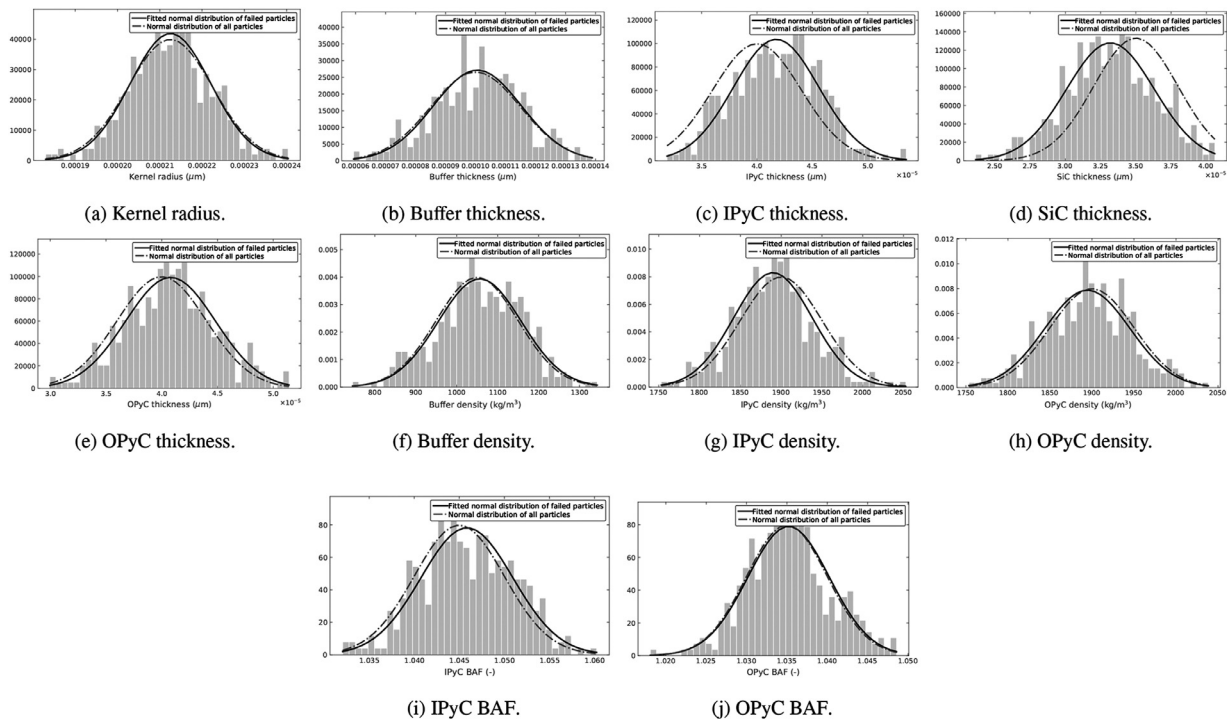


Fig. 13. Normalized histograms of statistically varied parameters for failed particles in AGR-5/6/7 Compact 5-1-3. Superimposed on these plots are fitted normal distributions of the parameters for the failed particles and for all particles.

Table 20

Parameters used in modeling the AGR-2 irradiation.

Category	Parameter	Nominal values \pm Standard Deviation
Fuel characteristics	^{235}U enrichment (wt%)	14.029
	Carbon/uranium (atomic ratio)	0.392
	Oxygen/uranium (atomic ratio)	1.428
Particle geometry	Kernel diameter (μm)	426.7 ± 8.8
	Buffer thickness (μm)	98.9 ± 8.4
	IPyC thickness (μm)	40.4 ± 2.5
	SiC thickness (μm)	35.2 ± 1.2
	OPyC thickness (μm)	43.4 ± 2.9
Fuel properties	Kernel density (g/cm^3)	10.966
	Kernel theoretical density (g/cm^3)	11.37
	Buffer density (g/cm^3)	1.05
	Buffer theoretical density (g/cm^3)	2.25
	IPyC density (g/cm^3)	1.89 ± 0.0011
	OPyC density (g/cm^3)	1.907 ± 0.007
	IPyC BAF	1.0465 ± 0.0049
	OPyC BAF	1.0429 ± 0.0019

ens the IPyC cracking probability. Similar findings were made in a sensitivity study on TRISO failure probability [33].

5.3. AGR-2 irradiation as-run prediction

The AGR-2 experiment was the second irradiation experiment performed under DOE's AGR program. The objective of AGR-2 was to irradiate both UCO and UO_2 TRISO fuel to obtain normal-operation and accident-condition fuel performance data [34,35]. The AGR-2 experiment was irradiated for 559.2 effective full power days (EFPD). BISON models use volume-averaged compact daily temperatures as boundary conditions at the outer edge of the OPyC layer. Use of daily temperatures can largely reflect the thermal state of the compacts throughout irradiation, thereby predicting accurate fission product diffusion and release. The TRISO UCO particle geometry and material properties are listed in Table 20. The findings of the study described in Section 5.2 and those reported

Table 21

Stress correlation factors and effective mean strength of AGR-2 Compacts 5-1-3, 5-3-3, 6-4-2, and 6-4-3.

Compact	Intact	IPyC cracking		Asphericity		
	$\sigma_{ms}(\text{MPa})$	$\sigma_{ms}(\text{MPa})$	$\frac{\hat{\sigma}_{2D}}{\hat{\sigma}_{1D}}$	$\sigma_{ms}(\text{MPa})$	$\frac{\hat{\sigma}_{2D}}{\hat{\sigma}_{1D}}$	$\frac{\Delta\hat{\sigma}_{2D}}{\Delta\hat{\sigma}_{1D}}$
5-1-3	720	1363	-1.19	1055	1.39	1.21
5-3-3	711	1362	-1.239	1063	1.41	1.24
6-4-2	708	1199	-0.94	1027	1.47	1.26
6-4-3	708	1199	-0.97	1012	1.51	1.27

Table 22

Failure probability for AGR-2 Compacts 5-1-3, 5-3-3, 6-4-2, and 6-4-3.

Compact	IPyC cracking	SiC failure
5-1-3	2.23×10^{-1}	9.75×10^{-5}
5-3-3	1.25×10^{-1}	4.53×10^{-5}
6-4-2	3.59×10^{-1}	1.16×10^{-4}
6-4-3	3.15×10^{-1}	1.12×10^{-4}

in [33] on the effects of randomizing various parameters regarding the failure probability of AGR-5/6/7 particles indicate that variation in fuel properties has little impact on the failure probability of TRISO fuel. Thus, in these AGR-2 calculations, only statistical variations in fuel particle geometry as listed in Table 20 are considered.

Failure probability calculations are performed here using BISON on four AGR-2 compacts: 5-1-3, 5-3-3, 6-4-2, and 6-4-3. For these compacts, histories of the inner-wall tangential stresses in the SiC of an intact particle, a particle with IPyC cracking, and an aspherical particle are plotted in Fig. 14. The evolution of the buffer outer and IPyC inner radii and the buffer-IPyC gap are plotted in Fig. 15. Spikes on those curves are mainly caused by fluctuations in daily temperature history.

The stress correlation factors and effective mean strength are provided in Table 21. Table 22 summarizes the failure probabilities of IPyC cracking and SiC failure. The SiC failures of all four compacts are due to IPyC cracking, causing localized tensile

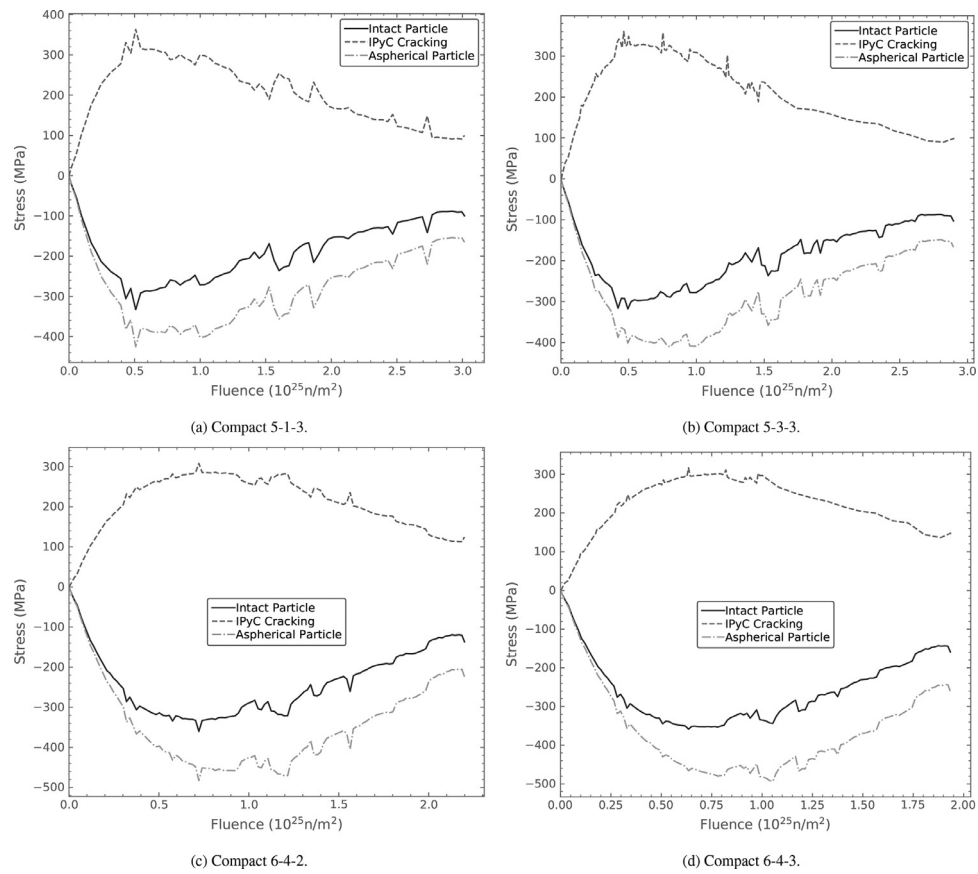


Fig. 14. Inner-wall tangential stress histories in the SiC layer for AGR-2 Compacts 5-1-3, 5-3-3, 6-4-2, and 6-4-3.

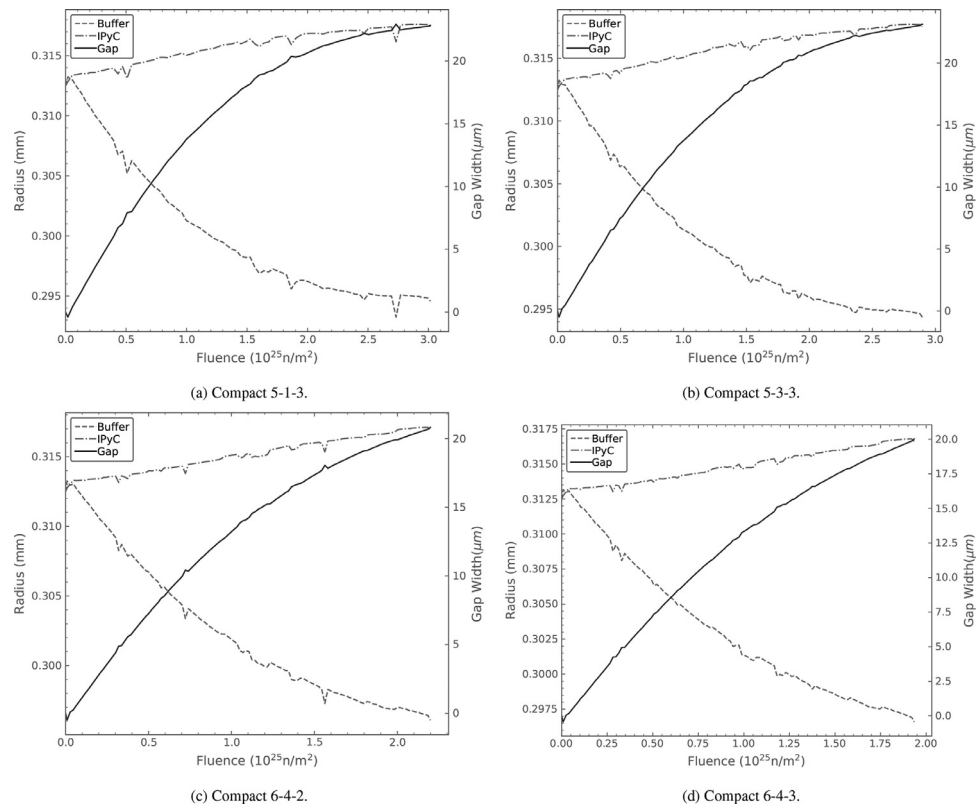


Fig. 15. Buffer outer and IPyC inner radii histories for AGR-2 Compacts 5-1-3, 5-3-3, 6-4-2, and 6-4-3. Gap size is computed as the difference between these radii.

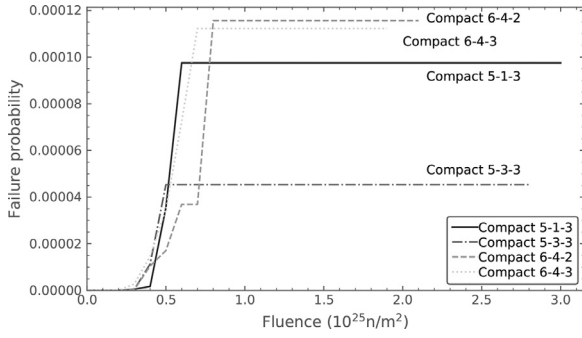


Fig. 16. Evolution of SiC failure probability in AGR-2 Compacts 5-1-3, 5-3-3, 6-4-2, and 6-4-3.

stress in the SiC layer. The evolution of SiC failure probability in Fig. 12 shows that particle failure occurs in the early phase of irradiation, when IPyC layers reach a maximum tension from shrinkage.

Fission product diffusion calculations are also performed here using BISON. For these calculations, mechanics balance equations are not solved, because the mechanical deformation has a minor effect on the diffusion process. The concentrations of silver, cesium, and strontium for an intact particle in Compact 5-1-3 at various times are plotted in Fig. 17. For silver, the SiC layer is the main retention barrier, so a sharp drop in concentration occurs at the IPyC-SiC interface. Similarly, the SiC layer is also the main retention barrier for cesium. However, the kernel is more retentive of cesium than silver, due to the lower diffusivity of cesium in the kernel. Unlike with cesium and silver, for strontium, the kernel is the primary retention barrier. The concentration of strontium drops dramatically at the interface between the kernel and buffer, and little strontium is released from the kernel. This is due to a very low diffusion coefficient for strontium in the kernel.

Differences in silver, cesium, and strontium diffusion between an intact and a failed particle in Compact 6-1-3 can be seen in Fig. 18. The diffusion coefficient of the SiC layer in a failed particle is set to the non-retentive value of $1 \times 10^{-6} \text{ m}^2/\text{s}$. For silver and cesium in the intact case, the concentration drops dramatically across the SiC layer, while a failed SiC layer is no longer effective in retaining them. However, for strontium, the intact and failed results are indistinguishable. This is because the kernel retains nearly all the strontium. Strontium release is less affected by failure of the SiC layer.

Post-irradiation examination (PIE) was performed on the AGR-2 compacts to measure the release fractions of silver, cesium, and strontium. In BISON, the release fraction is obtained by dividing the release from a particle by the total inventory produced during irradiation. Since the diffusivities of these species in the graphite matrix are assumed to be high, it provides very low retention. Thus, the release from the compact is identical to the release from all the particles. The experimentally measured release fractions of

silver are compared to BISON and PARFUME's predictions in Fig. 19. As seen from the figure, the BISON results compare very favorably with those of PARFUME [36], though they both underpredict PIE release fractions [37].

The evaluation of cesium and strontium release for Compact 5-3-3 assumes that there is one failed particle, according to an analysis of fission products from Deconsolidation-Leach-Burn-Leach (DLBL) [38]. The release fraction is computed as:

$$f = \frac{f_i(n - n_f) + f_f n_f}{n} \quad (62)$$

where f is the release fraction, f_i is the release fraction from the intact particle, f_f is the release fraction from the failed particle, n is the total number of particles in the compact, and n_f is the number of failed particles in the compact. For Compact 5-3-3, there are a total of 3176 particles. In this calculation, Monte Carlo simulation is not performed to account for any variations of the fuel properties and geometry. The f_i and f_f are simply computed for one intact and one failed particle, respectively.

The results for cesium and strontium release are plotted in Fig. 20. Both BISON and PARFUME [36] compute a higher release than seen in PIE for cesium. Compared to PARFUME, BISON predicts a higher release for strontium. This is because BISON does not model any diffusion in the graphite matrix, while PARFUME predicts some amount of strontium retention in the graphite matrix, due to its relatively low diffusivity. It is worthwhile to mention that BISON can model the fuel element in which TRISO particles are embedded; modeling of the diffusion in the graphite matrix will be considered in a future study.

6. Conclusion

The capabilities of BISON have been significantly expanded to enable it to model the fuel performance of TRISO particles. Recent developments include additional TRISO UCO material models, including models for mechanical response (elastic, creep, irradiation strain), thermal transport (thermal conductivity, specific heat), mass diffusion, and fission gas production and release. A new capability was developed to enable Monte Carlo sampling of a population of TRISO particles in order to account for the particle-to-particle statistical variations in physical dimensions and fuel properties that arise from the fuel fabrication process. This capability is essential for understanding the collective source term from the billions of particles present in a reactor. This capability relies on Weibull analysis, 2-D and 3-D analysis of failure modes, the ability to tie those higher-dimensional failure modes to fast-running 1-D analyses, and parallel computing.

These capabilities have been tested extensively, as documented here. A benchmark problem was used to compare BISON and PARFUME. Results show good agreement in terms of computed stresses and failure probabilities. BISON was then used to simulate three compacts in the AGR-5/6/7 irradiation test and compute their fail-

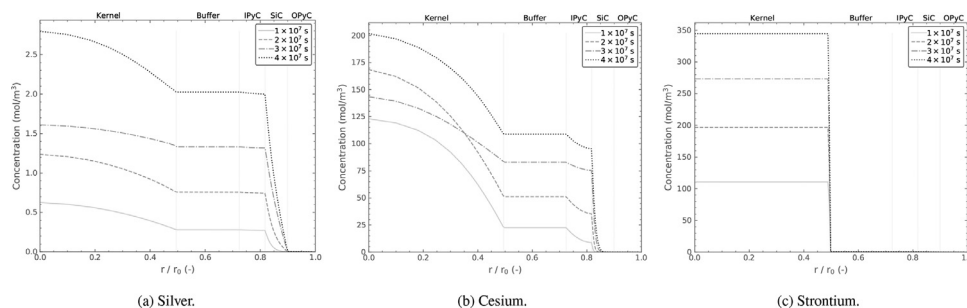


Fig. 17. Concentration profiles of fission products in AGR-2 Compact 5-1-3 at various points in time.

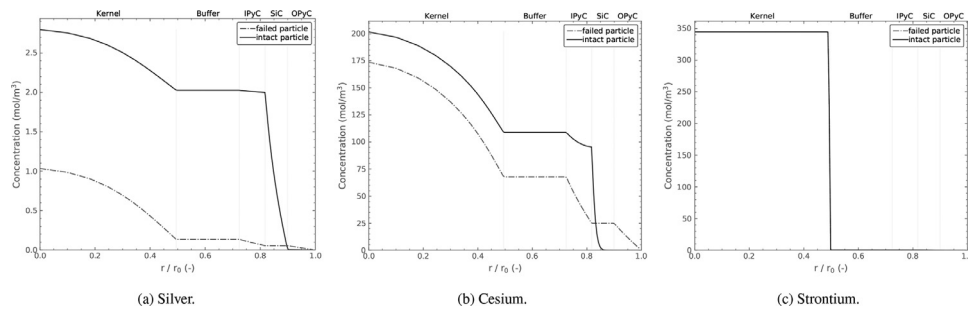


Fig. 18. Concentration profiles of fission products for an intact and a failed particle in AGR-2 Compact 5-1-3 at 4×10^7 seconds.

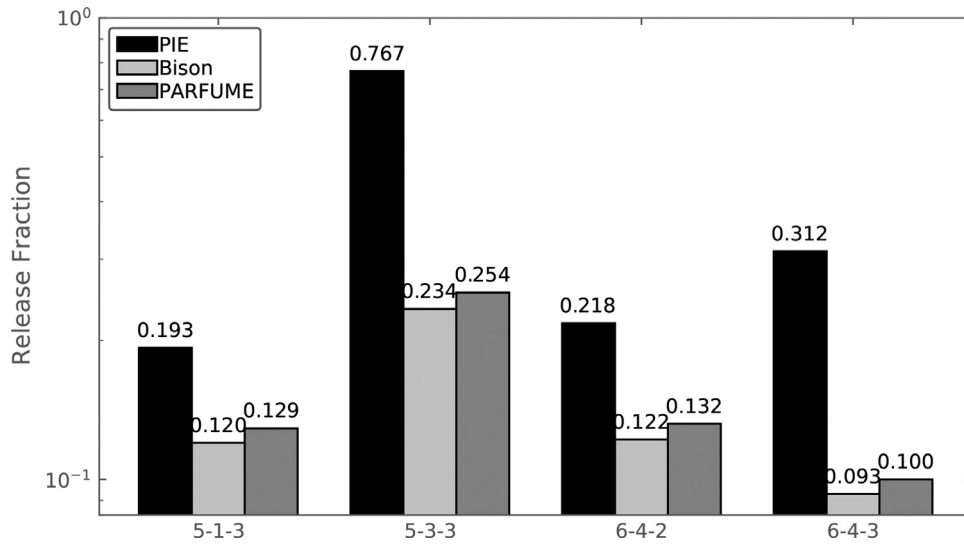


Fig. 19. Comparison of measured and computed silver release fractions among PIE, BISON, and PARFUME for AGR-2 Compacts 5-1-3, 5-3-3, 6-4-2, and 6-4-3.

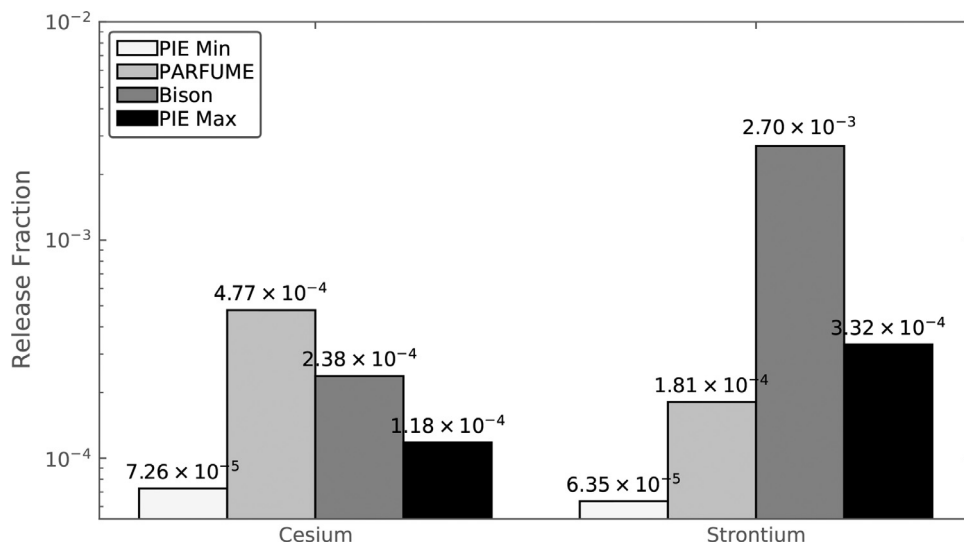


Fig. 20. Comparison of measured and computed cesium and strontium release fractions among PIE, BISON, and PARFUME for AGR-2 Compact 5-3-3. PIE Max and Min are the DLBL maximum and minimum experimental data [36].

ure probabilities. The statistics of the failed particles indicate that IPyC and SiC thickness significantly affect particle failure. Lastly, BISON was used to analyze four compacts in AGR-2 under its as-run irradiation conditions. In addition to a failure probability calculation, fission product diffusion was investigated for an intact parti-

cle and a failed particle. Fission release fractions for silver, cesium, and strontium were computed, and the BISON results compare favorably with those computed by PARFUME.

Future work will involve simulating other failure modes and incorporating them into the current Monte Carlo scheme. A fast-running approach for calculating failure probability will be devel-

oped to handle low failure probability cases for which Monte Carlo requires a very large sample size. Additional developments will add graphite matrix diffusion to fission product release calculations and include them in statistical failure analysis.

Declaration of Competing Interest

The authors declare that they have no known competing financial interests or personal relationships that could have appeared to influence the work reported in this paper.

CRediT authorship contribution statement

Wen Jiang: Conceptualization, Methodology, Software. **Jason D. Hales:** Methodology, Software, Writing - review & editing. **Benjamin W. Spencer:** Methodology, Software, Writing - review & editing. **Blaise P. Collin:** Methodology, Writing - review & editing. **Andrew E. Slaughter:** Methodology, Software, Writing - review & editing. **Stephen R. Novascone:** Software, Validation, Writing - review & editing. **Aysenur Toptan:** Software, Validation, Writing - review & editing. **Kyle A. Gamble:** Software, Validation, Writing - review & editing. **Russell Gardner:** Software, Validation, Writing - review & editing.

Acknowledgments

This manuscript has been authored by Battelle Energy Alliance, LLC under Contract No. DE-AC07-05ID14517 with the US Department of Energy, with funding from the Nuclear Energy Advanced Modeling and Simulation program (NEAMS), the Advanced Reactor Technologies program (ART) and the U.S. Industry Opportunities for Advanced Nuclear Technology Development Announcement No: DE-FOA-0001817. The U.S. Government retains and the publisher, by accepting the article for publication, acknowledges that the U.S. Government retains a nonexclusive, paid-up, irrevocable, worldwide license to publish or reproduce the published form of this manuscript, or allow others to do so, for U.S. Government purposes.

This research made use of the resources of the High Performance Computing Center at Idaho National Laboratory, which is supported by the Office of Nuclear Energy of the U.S. Department of Energy and the Nuclear Science User Facilities under Contract No. DE-AC07-05ID14517.

References

- [1] P.A. Demkowicz, B. Liu, J.D. Hunn, Coated particle fuel: historical perspectives and current progress, *J. Nucl. Mater.* 515 (2019) 434–450, doi:10.1016/j.jnucmat.2018.09.044.
- [2] Uranium oxycarbide (UCO) tristructural isotropic (TRISO) coated particle fuel performance: Topical Report EPRI-AR-1(NP), 2019.
- [3] K. Verfondern, H. Nabelek, PANAMA A computer code to predict TRISO particle failure under accident conditions, Technical Report Juel-Spez-298, Germany, 1985.
- [4] D.G. Martin, Considerations pertaining to the achievement of high burn-ups in htr fuel, *Nucl. Eng. Des.* 213 (2002) 241–258.
- [5] M. Phelip, F. Michel, M. Pelletier, G. Degeneve, P. Guillermier, The ATLAS HTR fuel simulation code objectives, description and first results, in: 2nd International Topical Meeting on High Temperature Reactor Technology, 2004, pp. 1–10, Beijing, China.
- [6] A. Xhonneux, H.-J. Allelein, Development of an integrated fission product release and transport code for spatially resolved full-core calculations of v/htrs, *Nuclear Engineering and Design* 271 (2014) 361–369. SI: HTR 2012
- [7] G.K. Miller, D.A. Petti, J.T. Maki, D.L. Knudson, W.F. Skerjanc, PARFUME Theory and Model Basis Report, Report, INL/EXT-08-14497 (Rev.1), Idaho National Laboratory, 2018.
- [8] J. Wang, An Integrated Performance Model for High Temperature Gas Cooled Reactor Coated Particle, Massachusetts Institute of Technology, 2004 Ph.D. thesis.
- [9] A Review of Radionuclide Release from HTGR Cores During Normal Operation, Technical Report, 1009382, EPRI.
- [10] J.J. Powers, B.D. Wirth, A review of TRISO fuel performance models, *J. Nuclear Materials* 405 (1) (2010) 74–82, doi:10.1016/j.jnucmat.2010.07.030.
- [11] N. Baghdasaryan, T. Kozłowski, Review of progress in coated fuel particle performance analysis, *Nucl. Sci. Eng.* 194 (3) (2020) 169–180.
- [12] R.L. Williamson, J.D. Hales, S.R. Novascone, G. Pastore, K.A. Gamble, B.W. Spencer, W. Jiang, S.A. Pitts, A. CasAGRanda, D. Schwen, A.X. Zabriskie, A. Toptan, R.J. Gardner, C. Matthews, W. Liu, H. Chen, BISON: A flexible code for advanced simulation of the performance of multiple nuclear fuel forms, *Nuclear Technology* (accepted).
- [13] J.D. Hales, R.L. Williamson, S.R. Novascone, D.M. Perez, B.W. Spencer, G. Pastore, Multidimensional multiphysics simulation of TRISO particle fuel, *J. Nucl. Mater.* 443 (1) (2013) 531–543, doi:10.1016/j.jnucmat.2013.07.070.
- [14] BISON documentation, (<https://mooseframework.inl.gov/bison/>).
- [15] J. Fink, Thermophysical properties of uranium dioxide, *J. Nucl. Mater.* 279 (2000) 1–18.
- [16] D.R. Olander, Fundamental aspects of nuclear reactor fuel elements, Technical Information Center, Energy Research and Development Administration, 1976.
- [17] F. Ho, NP-MHTGR: Material Models of Pyrocarbon and Pyrolytic Silicon Carbide, Report, CEGA-002820 Rev. 1, CEGA Corporation, 1993.
- [18] V. Barabash, I. Mazul, R. Latypov, A. Pokrovsky, C. Wu, The effect of low temperature neutron irradiation and annealing on the thermal conductivity of advanced carbon-based materials, *J. Nucl. Mater.* 307–311 (2002) 1300–1304, doi:10.1016/S0022-3115(02)00961-3.
- [19] D. Petti, P. Martin, M. Phelip, R. Ballinger, Development of Improved Models and Designs for Coated-Particle Gas Reactor Fuels, Technical Report, INL/EXT-05-02615, Idaho National Engineering and Environmental Laboratory, 2004.
- [20] L.L. Snead, T. Nozawa, Y. Katoh, T.-S. Byun, S. Kondo, D.A. Petti, Handbook of SiC properties for fuel performance modeling, *J. Nucl. Mater.* 371 (2007) 329–377.
- [21] I.J. van Rooyen, M.L. Dunzik-Gougar, P.M. van Rooyen, Silver (ag) transport mechanisms in TRISO coated particles: a critical review, *Nucl. Eng. Des.* 271 (2014) 180–188, doi:10.1016/j.nucengdes.2013.11.029.
- [22] B.P. Collin, D.A. Petti, P.A. Demkowicz, J.T. Maki, Comparison of silver, cesium, and strontium release predictions using PARFUME with results from the AGR-1 irradiation experiment, *J. Nucl. Mater.* 466 (2015) 426–442, doi:10.1016/j.jnucmat.2015.08.033.
- [23] Fuel performance and fission product behavior in gas cooled reactors Technical Report, IAEA-TECDOC-978, IAEA, 1997.
- [24] U. Littmark, J. Ziegler, Handbook of Range Distributions for Energetic Ions in All Elements, Technical Report, Pergamon Press, 1980.
- [25] A.H. Booth, A Method of Calculating Gas Diffusion from UO₂ Fuel and its Application to the X-2-f Loop Test, Technical Report, AECL-496, Atomic Energy of Canada Ltd., 1957.
- [26] J.A. Turnbull, C.A. Friskney, J.R. Findlay, F.A. Johnson, A.J. Walter, The diffusion coefficients of gaseous and volatile species during the irradiation of uranium dioxide, *J. Nucl. Mater.* 107 (1982) 168–184.
- [27] R.L. Williamson, J.D. Hales, S.R. Novascone, M.R. Tonks, D.R. Gaston, C.J. Permann, D. Andrs, R.C. Martineau, Multidimensional multiphysics simulation of nuclear fuel behavior, *J. Nucl. Mater.* 423 (1) (2012) 149–163, doi:10.1016/j.jnucmat.2012.01.012.
- [28] C.J. Permann, D.R. Gaston, D. Andr, R.W. Carlsen, F. Kong, A.D. Lindsay, J.M. Miller, J.W. Peterson, A.E. Slaughter, R.H. Stogner, R.C. Martineau, MOOSE: Enabling massively parallel multiphysics simulation, *SoftwareX* 11 (2020) 100430, doi:10.1016/j.softx.2020.100430.
- [29] W. Jiang, B.W. Spencer, J.E. Dolbow, Ceramic nuclear fuel fracture modeling with the extended finite element method, *Eng Fract Mech* 223 (2020) 106713, doi:10.1016/j.engfracmech.2019.106713.
- [30] D.R. Gaston, C.J. Permann, J.W. Peterson, A.E. Slaughter, D. Andrš, Y. Wang, M.P. Short, D.M. Perez, M.R. Tonks, J. Ortensi, L. Zou, R.C. Martineau, Physics-based multiscale coupling for full core nuclear reactor simulation, *Ann Nucl Energy* 84 (2015) 45–54.
- [31] Advances in High Temperature Gas Cooled Reactor Fuel Technology Technical Report, IAEA-TECDOC-CD-1674, IAEA, 2012.
- [32] B.P. Collin, AGR-5/6/7 Irradiation Experiment Test Plan, Report, MIS-17-43095 (Rev.1), Idaho National Laboratory, 2018.
- [33] W.F. Skerjanc, J.T. Maki, B.P. Collin, D.A. Petti, Evaluation of design parameters for TRISO-coated fuel particles to establish manufacturing critical limits using PARFUME, *J. Nucl. Mater.* 469 (2016) 99–105, doi:10.1016/j.jnucmat.2015.11.027.
- [34] B. Collin, AGR-2 Irradiation Test Plan, Report, PLN-3798 (Rev.2), Idaho National Laboratory, 2018.
- [35] B. Collin, AGR-2 Irradiation Test Final As-Run Report, Report, INL/EXT-14-32277 (Rev.4), Idaho National Laboratory, 2018.
- [36] W.F. Skerjanc, Comparison of Fission Product Release Predictions Using PARFUME With Results From the AGR-2 Irradiation Experiment, Technical Report, INL/EXT 20 59448 (Rev.0), Idaho National Laboratory, 2020.
- [37] J.D. Stempien, J.M. Harp, P.A. Demkowicz, Fission Product Inventory and Burnup Evaluation by Gamma Spectrometry of the AGR 2 Irradiation, Technical Report, INL/EXT 16 39777 (Rev.1), Idaho National Laboratory, 2020.
- [38] J.D. Hunn, R.N. Morris, F.C. Montgomery, T.J. Gerczak, D.J. Skitt, C.A. Baldwin, J.A. Dyer, G.W. Helmreich, B.D. Eckhart, Z.M. Burns, P.A. Demkowicz, J.D. Stempien, Post-irradiation examination and safety testing of us AGR-2 irradiation test compacts, in: Proceedings of the HTR 2018 Conference, 2018. Warsaw, Poland.